RSC Advances

PAPER

View Article Online
View Journal | View Issue

Cite this: *RSC Adv.*, 2026, **16**, 4392

Enhanced hydrophilic properties and performance evaluation of PVDF-TiO_2-nZVI-SiO_2 nanocomposite membranes for the remediation of heavy metal contaminated wastewater

Murtala Namakka, *[ab] Md Rezaur Rahman, [a] Khairul Anwar Bin Mohamed Said[a] and Bavya Devi Karuppasamy[c]

Exposure to heavy metal contaminated water causes irreversible harm to humans and the environment. Despite the recent progress in nanofiltration for heavy metal remediation, advanced innovations are necessary to improve its effectiveness and membrane hydraulic performance. In this article, a hydrophilic multifunctional PVDF-TiO_2-nZVI-SiO_2 nanocomposite membrane material was developed using a phase inversion technique for the remediation of lead and hexavalent chromium contaminants. The synthesized TiO_2-nZVI-SiO_2 nanocomposite and PVDF-TiO_2-nZVI-SiO_2 nanocomposite membranes were characterized *via* various characterization techniques including FESEM, FTIR, EDX, XRD, XPS, TGA, water contact angle, and solvent content analysis. The novel TiO_2-nZVI coated SiO_2 nanocomposite membranes were fabricated by varying TiO_2-nZVI-SiO_2 nanocomposite loadings from 0.1 g (M1) to 0.3 g (M5) and the optimal modification was determined *via* detailed performance evaluation under varying concentrations *viz.* 20 ppm, 30 ppm, 40 ppm and 50 ppm. The removal efficiencies of the PVDF- TiO_2-nZVI-SiO_2 membranes were consistently stable despite increase in nanocomposite loadings with optimum membrane (M5) achieving 99.8% removal efficiency during the 50 minutes filtration operation. The TiO_2-nZVI-SiO_2 nanocomposite combines synergistic redox reaction and hydrophilic properties *via* TiO_2-nZVI and stabilization against particle aggregation from the surface SiO_2. Long-term stability study, the influence of contaminant type and loading on PVDF- TiO_2-nZVI-SiO_2 membrane and hydraulic performance corroborated sustained hydraulic properties and stable performance exceeding 90% across all contaminant loadings.

Received 12th November 2025
Accepted 27th December 2025

DOI: 10.1039/d5ra08723f

rsc.li/rsc-advances

1 Introduction

Lack of safe drinking water due to contamination from harmful inorganic and organic chemicals has been declared a global concern by the United Nations since 2023, threatening 26% of the global population. Amid the current surge of global population and technological advancements, the demand for sustainable water and energy security is never more crucial than now. However, the global demand of clean water, free of harmful contaminants, for human consumption, food and energy security will likely be overstretched by the recent advancements in AI technologies and Data Centres which utilise large-scale computational models that require clean water for thermal management.[1] The water used for cooling data centres to maintain optimum operations of these technologies, is often sourced from municipal water supplies adding to a compounding environmental concern.[1,2] These make the development of effective materials for the treatment of industrial effluents and other wastewater sources highly critical. Efficient wastewater purification technologies capable of removing emerging contaminants such as dyes,[3,4] emulsions[5] and heavy metals[6] are sustainable alternatives for the increasing water demands. Heavy metal pollution is a contemporary environmental challenge associated with the discharge of heavy metals into water systems from industrialisation and rapid urban developments. Recent studies have investigated the harmful effects of heavy metal contaminants such as arsenic,[7,8] cadmium,[9,10] chromium[11,12] and lead.[13,14] Despite the remediation intervention, heavy metal contaminations remain a significant concern. One of the most complex heavy metal contaminations is the hexavalent chromium, Cr(VI) contamination which often occur from soil or volcanic dust sources. Cr(VI) is highly toxic, carcinogenic, corrosion resistance with relatively high melting points compared to Cr(III) oxidation state which forms insoluble hydroxides when exposed to water.[11,15]

[a]*Department of Chemical Engineering and Energy Sustainability, Universiti Malaysia Sarawak, Malaysia. E-mail: abuhuzaifah33@yahoo.com; rmrezaur@unimas.my*
[b]*Department of Chemical Engineering, Ahmadu Bello University Zaria-Nigeria, Nigeria*
[c]*KPR Institute of Engineering and Technology, India*

Lead Pb^{2+} contamination has been reported to inadequately affect ecosystem due to its enormous toxicity,[16] with current available remediation techniques lacking sustainability.[16,17] Therefore, new remediation materials and strategies for the removal of lead and hexavalent chromium(VI) are essential in mitigating potential health hazards and future environmental contaminations. Conventional methods such as chemical precipitation,[18,19] ion exchange,[20,21] electrochemical[22,23] and adsorption methods are commonly employed with relative success.[24,25] Although limitations including selectivity in ion exchange, efficacy of resin generation, production of passive non-conductive layer in electrochemical method are a major drawback. Consequently, advanced oxidation processes coupled with the utilization of biological wastewater treatment strategies have been explored to enhance target ion selectivity while maintaining stable adsorption capacity.[22,23] Nevertheless, long operation time,[26] excessive sludge formation,[27] remains a challenge in adopting these strategies.[28,29] Hence, adsorption method remains the most widely employed approach for both lead and Cr(VI) remediation compared to other remediation strategies.[30,31] The efficiency of adsorption method significantly lies on the nature and catalytic activity of the adsorbent with iron and silica-based adsorbent recording the higher Cr(VI) adsorption capacity.[32] However, the approach requires post treatment cost coupled with unstable adsorption efficiency due to passivation of iron active sites after the chemical reduction of Cr(VI) to Cr(III) over time.[33–35]

To address this challenge, it is crucial to develop effective and sustainable remediation approach capable of preventing formation of passive layers and nanomaterial aggregation while efficiently combating the diverse range of toxic heavy metals from wastewater effluents.[16] Zero valent iron (ZVI) is characterized by its exceptional reactivity, injective ability and large surface area electron donor that reduces emerging contaminants.[36] However, individual nZVI can easily passivate or agglomerated thereby limiting overall performance. Researchers have reported enhanced stability of nZVI by incorporating it a support materials forming stable nanocomposite with less potential passivation properties shielding active nZVI surface particularly TiO_2 which is also a studied adsorbent capable of mineralizing heavy metal contaminants[37] with potential recombination. The coating of TiO_2-nZVI was reported with efficient dispersibility, reducing capacity, adsorption properties and a significant photocatalytic.[38]

In this study, an efficient, advanced adsorbent incorporated PVDF membrane was developed for removal of emerging Pb^{2+} and Cr(VI) contaminants. The synergistic combination of nZVI,[39] silica SiO_2, and TiO_2 have shown successful application in environmental remediation with recent application reporting 100% MB dye removal.[40] Previous studies utilize direct chemical reaction in the synthesis of nZVI-TiO_2-SiO_2. In the current study a layer-by-layer patter was adopted to systematically developed three layers of the nanocomposite by coating the TiO_2-nZVI with SiO_2 using CTAB to enable hierarchy in the nanocomposite structural interface. Subsequently, PVDF-TiO_2-nZVI-SiO_2 nanocomposite membrane was fabricated *via* phase inversion by varying the nZVI-TiO_2-SiO_2 nanocomposite concentration from 0.1 g to 0.30 g for M1 to M5. The nZVI-TiO_2-SiO_2 and nanocomposite membrane were characterized *via* various techniques. Performance of the nanocomposite membrane was assessed *via* various techniques including solvent content, water contact angle, water flux and the remediation of Pb^{2+} and Cr(VI) contaminants.

2 Materials and methods

2.1 Materials

For the fabrication of TiO_2-nZVI and SiO_2 coated nanocomposite, All procured Chemicals including Sodium borohyas procured, $FeSO_4 \cdot 7H_2O$, ethanol, CH_3CH_2OH, methanol CH_3OH, sodium hydroxide, NaOH, hydrochloric acid HCl, titanium oxide TiO_2 (CAS No: 13 463-67-7), Tetraethyl orthosilicate TEOS $Si(OC_2H_5)_4$, NH_3, 1-propanol C_3H_8O 99.5%, and Cetyltrimethylammonium Bromide CTAB, were used as procured from Sigma-Aldrich Sdn. Bhd. (Malaysia). Synthesized nZVI, and TiO_2-nZVI were prepared. Chemicals for nanocomposite membrane fabrication includes Poly vinylidene fluoride, (PVDF) (CAS No: 24 937-79-9, Mm 534 000 g mol^{-1}) as the primary polymer matrix for its intrinsic chemical resistivity and thermal stability, *N*-methyl-2-pyrrolidone (NMP) as a solvent to ensure a homogeneous dispersion of TiO_2-nZVI-SiO_2 nanoparticles in the casting solution. Throughout the experimental procedures, all aqueous reagent solutions were prepared with ultrapure water while industrial grade nitrogen, N_2 utilized in this work, was provided by Universiti of Malysia Sarawak.

2.2 Synthesis of TiO_2-nZVI nanoparticles

The TiO_2-nZVI nanocomposite was synthesized following the procedure described in ref. 41 and 37 with little modifications. Briefly, a precursor solution was prepared by dissolving 5.56 g of ferrous sulfate heptahydrate ($FeSO_4 \cdot 7H_2O$) and a specific amount of pre-synthesized TiO_2 nanoparticles in 200 ml of ultrapure water within a three-necked flask. The mixture was continuously purged with N_2 gas under constant stirring for 30 minutes to achieve a homogeneous, oxygen-free TiO_2–$FeSO_4$ solution. Sodium hydroxide (NaOH) and hydrochloric acid (HCl) (0.01 mol L^{-1}) were used to adjust the solution pH. Concurrently, sodium borohydride ($NaBH_4$) reducing agent solution was formulated by dissolving 1.60 g of NaBH4 in 50 ml deionized water. The reduction of ferrous ions, Fe^{2+} to zero valent iron Fe^0 on the TiO_2 particles was subsequently initiated by the dropwise addition of the $NaBH_4$ solution into the TiO_2–$FeSO_4$ solution (see eqn (1)–(3)).

$$FeSO_4 \cdot 7H_2O + 2NaBH_4 \rightarrow Fe^0 + NaSO_4 + 7H_2O + 2B(OH)_3 \quad (1)$$

$$Fe^{2+} + 2BH_4 - + 6H_2O \rightarrow Fe^0 + 2B(OH)_3 + 7H_2\uparrow \quad (2)$$

$$Fe^0 \rightarrow Fe^{2+} + 2e^- \quad (3)$$

The reaction was allowed to proceed for 25 minutes; the cessation of gas evolution and complete formation of black colored particles indicates quantitative reduction of Fe^{2+} to Fe^0.

The solution was allowed to settle for few minutes, washed several times using 95% ethanol to remove excess reactants and uncoated TiO_2 particles before centrifuging for 5 minutes at 20 000 rpm at room temperature. The binary composite was dried at 90 °C for 4 hours in a tube furnace under nitrogen condition. Dried TiO_2-nZVI nanoparticles were stored for further characterizations.

2.3 Synthesis of TiO_2-nZVI-SiO_2 nanoparticles

The TiO_2-nZVI-SiO_2 nanocomposites were synthesized by modifying the procedure described in ref. 42. Briefly, specified amount of TiO_2-nZVI- nanoparticles were prepared and ultrasonically dispersed in 75% ethanol solutions. The mixture was continuously sonicated before introducing 10 ml Ammonia and *n*-propanol with 2.1 g of cationic surfactant Cetyltrimethylammonium Bromide, CTAB solutions. Subsequently tetraethyl orthosilicate was added and the reaction was allowed to proceed at 85 °C for 6 hours. The silica coated TiO_2-nZVI nanoparticles were collected, washed several times with 75% ethanol and centrifuged for 5 minutes at 20 000 rpm under room temperature conditions. Subsequently, the particles were dried at 95 °C in a tube furnace and stored for further characterization and membrane fabrications.

2.4 Fabrication of TiO_2-nZVI-SiO_2 nanocomposite membranes

Polyvinylidene fluoride (PVDF) and NMP were used as the base polymer and PVDF solvent for the preparation of dope solutions, while synthesized TiO_2-nZVI-SiO_2 nanoparticles were incorporated into the membrane dope solution to enhance hydrophilicity, self-cleaning and overall performance of the nanocomposite membrane. The dope solutions were prepared following the procedure described in ref. 43 and 44 with the following modifications. Briefly, PVDF pellets (14% w v^{-1}) were added to a predetermined volume of NMP solvent in a 250 ml conical flask. TiO_2-nZVI-SiO_2 nanoparticles were subsequently introduced at varying concentrations *viz.* 0.1 g, 0.15 g, 0.20 g, 0.25 g and 0.30 g. The solutions were covered using foil paper and subjected to 350 rpm magnetic stirring at 85 °C for 24 hours to ensure effective dissolution and homogenous dispersion of the TiO_2-nZVI-SiO_2 nanoparticles in the dope solutions. To eliminate possibly entrapped air bubbles introduced during stirring, which could potentially introduce defects in the cast membrane, the homogenously dispersed dope solutions were transferred to an oven and held at 50 °C for 1 hour, this procedure reduces the solution viscosity and allows microbubbles to coalesce. Subsequently, the bubble-free dope solution (approximately 10 ml) was cast onto a clean, dry glass substrate (21 cm × 30 cm) using a doctor blade film applicator and immediately immersed in a coagulation bath containing deionized water maintained at room temperature (approximately 25 °C). This step helps initiate the non-solvent induced phase separation process, resulting in the solidification of the polymer solution and the formation of a hydrophilic TiO_2-nZVI-SiO_2 nanocomposite membrane. Following phase inversion, the nanocomposite membranes were transferred to another coagulation bath containing fresh deionized water for 12 hours (overnight). The coagulation bath water was replaced with fresh distilled water to ensure the complete extraction of residual NMP solvent and any soluble components from the TiO_2-nZVI-SiO_2 nanocomposite membrane matrix. Finally, the nanocomposite membranes were stored in a fridge for further analysis. Table 1 shows the TiO_2-nZVI-SiO_2 nanocomposite membrane designated code and compositions.

Table 1 Code and compositions of the fabricated TiO_2-nZVI-SiO_2 nanocomposite membranes

Code	PVDF (wt%)	Concentration of TiO_2-nZVI-SiO_2 (grams)	NMP solvent (v%)
Mo	14	0	86
M1	14	0.10	86
M2	14	0.15	86
M3	14	0.20	86
M4	14	0.25	86
M5	14	0.30	86

2.5 Characterizations

Synthesized TiO_2-nZVI, SiO_2 coated TiO_2-nZVI and fabricated nanocomposite membranes were characterized *via* XRD, FTIR, TGA, FESEM, EDX, and XPS analytical techniques to corroborate the physicochemical properties and chemical bonding of the synthesised nanocomposite material.

Fourier-transform infrared (FTIR) spectroscopy was performed using a Shimadzu IRAffinity-1 spectrometer to characterize the molecular bond structures and functional groups of the nanoparticles and the fabricated membranes. Both analyses were conducted in attenuated total reflectance (ATR) mode across a wavenumber range of 4000 to 400 cm^{-1}, with a spectral resolution of 4 cm^{-1} and an accumulation of 32 scans per spectrum. For measurement, a section of each sample was placed on the ATR crystal and secured with a swivel press to ensure optimal surface contact.

The surface morphology and elemental composition of the synthesized nanocomposites were characterized by using field emission scanning electron microscopy coupled with energy-dispersive X-ray spectroscopy (FESEM-EDS), which are well-established techniques for microstructural and elemental analysis.[45,46] The FESEM images (×15 000 and ×50 000 magnification) were acquired with a Hitachi S-4700 instrument, operating at an accelerating voltage of 20 kV, which illustrates the morphological structure of the TiO_2-nZVI, silica coated TiO_2-nZVI nanocomposites and modified PVDF- TiO_2-nZVI-SiO_2. Subsequently, the thermal stability of the TiO_2-nZVI and the influence of SiO_2 coating on the physicochemical properties of the synthesized TiO_2-nZVI-SiO_2 nanocomposite material was evaluated *via* TGA analysis under the following conditions: on set temperature of 323.69 °C, Inflect. Point temperature 372.92 °C, end set temperature 388.95 °C and midpoint 351.52 °C under constant N_2 supply. The XPS analysis was conducted to investigate the chemical bonding and elemental interactions within the nanocomposite material. The analysis followed the procedure described in ref. 47 and 48 and the

deconvolutions and peaks identification were guided by the standard procedure described in ThermoFisher scientific. Briefly. The analysis was carried out in Alpha-K XPS spectrometer using monochromatic aluminium radiation at 0.3 eV FWHM, 1.5% pass energy resolution and 11.75 eV to 23.5 eV measurement pass energy resolution as described in operation manual. The crystallinity and phase composition of the SiO_2 coated TiO_2-nZVI nanoparticles and the fabricated nanocomposite membranes were analysed using X-ray diffraction (XRD). Measurements were performed at ambient temperature on a Rigaku SmartLab Powder X-ray diffractometer. Data were collected over a 2θ angular range from 0° to 80°. The crystalline index (CrI), serving as a measure of the degree of crystallinity, was determined using the empirical equations described in ref. 49. The crystallite size was calculated using origin software (see S1CA 1–10), by employing Debye–Scherrer equation and the standard procedure of the ASTM F3419-22 (2022) standard.[50]

$$\text{Crystalline index}(\%) = \frac{A_c}{A_t} \times 100 \quad (4)$$

$$A_t = A_c + A_m \quad (5)$$

$$D = \frac{k\lambda}{\beta \cos \theta} \quad (6)$$

where A_c represent "Area of all the crystalline peak A_m represents the area of amorphous peaks A_t total area of all peaks k is the Scherrer constant = 0.94 λ (nm) is the X-ray wavelength = 1.5418 β (radians) represent the full width at half maximum, FWHM θ (Degree) is the Bragg angle.

2.6 Nanocomposite membrane performance analysis

2.6.1 Membrane porosity. The porosity of the TiO_2-nZVI-SiO_2 nanocomposite membranes were measured by recording the weight of the membrane piece before and after wetting. The wetted membrane was immersed in deionized water for 24 hours as described in ref. 51.

$$\varepsilon(\%) = \frac{\left(\frac{W_a - W_b}{\rho_w}\right)}{\left(\frac{W_a - W_b}{\rho_w}\right) + \left(\frac{W_b}{\rho_{PVDF}}\right)} \times 100 \quad (7)$$

where W_a and W_b are the weight of wet and dry membrane (g). ρ_w and ρ_{PVDF} are the density of water (0.998 g cm^{-3}) and PVDF polymer (1.740 g cm^{-3}).

2.6.2 Membrane hydrophilicity. The surface hydrophilicity of the fabricated TiO_2-nZVI-SiO_2 membranes was quantitatively evaluated through static water contact angle measurements, employing the sessile drop method with an Ossila contact angle goniometer. Ultrapure water was used as the probe liquid.[52] To ensure for surface heterogeneity, measurements were repeated randomly in different selected locations per sample. Influence of time on the water contact angle was evaluated. The reported contact angle value represents the arithmetic mean of these replicate measurements, providing a robust characterization of the macroscopic wetting characteristics.

2.6.3 Membrane solvent content analysis. The solvent uptake behavior and swelling characteristics of the TiO_2-nZVI-SiO_2 nanocomposite membrane were quantitatively analyzed to investigate the thermodynamic interactions between the polymer matrix and other polar solvents *viz.* Water, ethanol and methanol. Briefly, a piece of the TiO_2-nZVI-SiO_2 nanocomposite membrane with a uniform area of 1 cm^2 was cut and immersed in water, methanol and ethanol for 24 hours until equilibrium swelling was achieved, the weight of the membrane before and after wetting were measured. This approach was utilized by ref. 43 and 53. The degree of swelling was assessed gravimetrically by calculating the mass difference between the swollen equilibrated state, W_s and the dry state W_d. The equilibrium solvent content (S_c), expressed as a percentage, was then determined by the following mathematical expression.

$$S_c = \frac{W_s - W_d}{W_s} \times 100 \quad (8)$$

2.6.4 Membrane shrinkage ratio analysis. The shrinkage ratio is defined as the ratio of the volume of the dry membrane to that of the wet membrane. In this analysis, similar membrane sample size (1 cm^2) was used as in the case of solvent content analysis. However, only deionized water was used throughout herein. Initially, the length and thickness of the membrane were measured before wetting in deionized water for 1 day. Subsequently, the parameters were recalculated, and the shrinkage ratio was evaluated using the following mathematical expression described in ref. 54.

$$\text{Shrinkage ratio}(\%) S_r = \left[1 - \frac{(l_. \times b_.)}{(l_0 \times b_0)}\right] \times 100 \quad (9)$$

2.6.5 Membrane pure water flux analysis. The methodology described in ref. 55 was modified. Briefly, the nanocomposite membrane discs (4.4 cm diameter) were cut and installed in the filtration unit. After loading 2.5 L of pure water, the system was started at zero pressure. A stabilization period involved gradually increasing the pressure to 2.0 bars for 30 minutes. The system was then operated at 1.0 bar, with permeate volume measured at 5 minutes intervals over 65 minutes. Water permeation flux was calculated as described by Omar *et al.* (2023). For accuracy, the experiment was replicated for each membrane, and average flux values were determined using the following equation.

$$\text{Pure water flux}(J_w) = \frac{Q}{A\,\Delta T} \quad (10)$$

where Q is the amount of pure water that passes the nanocomposite membrane (m^3), ΔT is the filtration time (h), A is the membrane area (m^2).

2.6.6 Nanocomposite membrane heavy metal removal analysis. The heavy metal rejection performance of the nanocomposite membranes was evaluated with aqueous solutions of Cr(VI), and Pb^{2+} at varying concentrations. Initially, 10 ppm single ion aqueous solutions of Pb^{2+} were prepared for the first filtration cycle for all the nanocomposite membranes (Mo, M1, M2, M3, M4 and M5) to determine the membrane with

optimum performance. Subsequently, the optimum membrane was subjected to the varying Pb^{2+} and Cr(IV) concentrations (20 ppm, 30 ppm, 40 ppm and 40 ppm) to evaluate the influence of heavy metal concentration on the overall nanocomposite membrane performance. Each of the filtration experiments were conducted at 1 bar and 25 °C for 70 minutes. Prior to testing, a preconditioning protocol described in water flux analysis was implemented, wherein the nanocomposite membrane was compacted at 2 bar for 20 minutes, followed by a 10 minutes stabilization period with the heavy metal solution at the same pressure to ensure structural stability and prevent artificially high initial rejection values. The feed solution was refilled continuously to maintain consistent feed concentrations. The concentration of heavy metal ions in the permeate was analyzed using atomic absorption spectroscopy (AAS) calibrated with a standard curve. The heavy metal rejection rate (R) was determined according to the following equation:[56]

$$R(\%) = \left[1 - \left(\frac{C_p}{C_f}\right)\right] \times 100 \quad (11)$$

3 Results and discussion

3.1 FTIR of nZVI, TiO_2-nZVI, and TiO_2-nZVI-SiO_2 nanocomposite

Fourier transform infrared spectroscopy with attenuated total reflectance (FTIR-ATR) was employed to characterize the functional groups present in the synthesized nZVI, nZVI-TiO_2, and TiO_2-nZVI-SiO_2 nanoparticles (Fig. 1). The spectra for all three nanoparticles exhibited characteristic absorption peaks correlated with the vibrational modes of their constituent chemical bonds. The FTIR spectra of the nZVI (a) and nZVI coated TiO_2 (b) nanoparticles were nearly identical, indicating that the composite is predominantly composed of the coated nZVI surface layer. In the FTIR spectrum of the TiO_2-nZVI composite, a broad absorption band observed at 3400.23 cm^{-1} is attributed to O–H stretching vibrations, which is consistent with the typical range for this functional group.[57] The peaks at 1590.78 cm^{-1} and 2104 cm^{-1} collectively suggest the presence of O–H bonds associated with the formation of α-FeOOH.[58,59] Furthermore, a shift in the Ti–O–Ti stretching vibration absorption band from 720 cm^{-1} to a lower wavenumber of 516.09 cm^{-1} corroborate the successful compositional integration of nZVI in TiO_2 surface layer.

In FTIR analysis of TiO_2-nZVI-SiO_2 shown in (c), both peak at 1030, –OH tensile vibration peak (2104 cm^{-1}), and –OH stretching (3400 cm^{-1}), peaks became sharp with a clear C–H vibrations around 2800 cm^{-1}, this can be associated with the surface coating by SiO_2 nanoparticles on the TiO_2-ZVI, thereby increasing the overall –OH functional group on the TiO_2-nZVI-SiO_2 nanocomposite material.

The effective encapsulation of TiO_2-nZVI within a silica matrix is essential for maintaining stability and reactivity, coupled with reduced passivation potential of nZVI surfaces, particularly in aqueous environments. Similar findings were reported in ref. 60. Moreover, the silica coating has been shown to mitigate the oxidation of nZVI, a factor critical for preserving its reductive capabilities. The vibrational nodes for the metal–oxygen bonds (Ti–O–Ti and Fe–O) were identified in the 484–500 cm^{-1} range, which are critical for the structural support of nZVI by TiO_2 40, amorphous SiO_2 peak with Si–O bending vibrations was noted at 680 cm^{-1}.[61,62] At little higher wavenumbers, the absorption bands between 1000 and 1006 cm^{-1} were assigned to Si–O–Ti or Si–O–Si asymmetric stretching vibrations.[63–65] The presence of surface hydroxyl groups, vital for the material's adsorptive and catalytic properties, was confirmed by multiple vibration intensities in both nanoparticle samples. These included Fe–O vibrations (500–742 cm^{-1}), O–H bending at 1630 cm^{-1}, more profound for TiO_2-

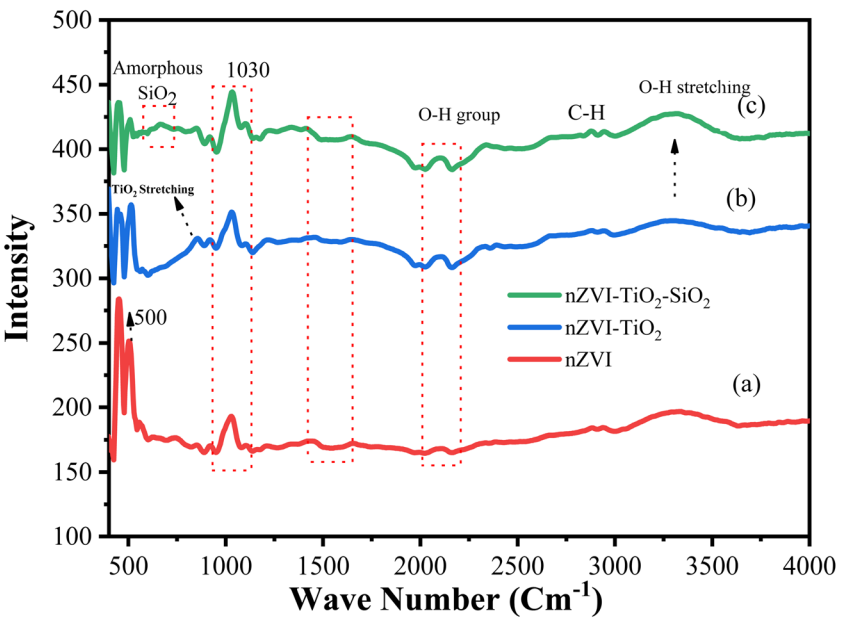

Fig. 1 FTIR of the synthesized nZVI, TiO_2-nZVI, and TiO_2-nZVI-SiO_2 nanoparticles.

nZVI, and coated SiO_2 sample, and O–H stretching nodes related to Fe–OH, Si–OH and Ti–OH species at 600 cm^{-1}, and 3400 cm^{-1} respectively. A comparative spectral analysis of the nanoparticles showed consistent peaks profiles, suggesting a stable composite structure.

3.2 FESEM/EDS analysis of TiO_2-nZVI-SiO_2 nanocomposite

Fig. 2 depicts the FESEM images at ×15 000 and ×50 000 magnification of the morphological structure of TiO2-nZVI and the silica coated TiO_2-nZVI nanocomposites. As shown in Fig. 2(a). The morphological structure of the TiO_2-nZVI nanoparticles, examined at a magnification of ×50 000 magnification reveals a regular spherical shape with a moderately uniform distribution of particles. Similar characteristic morphology was reported by Huang *et al.* (2018). In Fig. 2(b) under magnifications of ×15 000, the silica coated TiO_2-nZVI nanoparticle material, despite the homogeneity observed in TiO_2-nZVI (Fig. 2(a)), exhibits few irregularly shaped particles with a non-uniform distribution, this characteristic morphological property was also observed in previous research findings[41] indicating the presence of mesopores a morphological trait commonly associated with silica coated nZVI-based nanocomposites.[66,67]

The ×50 000 magnified view in image (c) elucidates a detailed particle morphology. The relatively uniform surface morphology observed suggests an efficient silica coating, as supported by previous studies that highlight the benefits of silica for enhancing the dispersibility and stability of metal nanoparticles.[60,63] Fig. 3 shows the elemental compositions of the synthesized nanocomposite material, from this figure, energy-dispersive X-ray spectroscopy (EDS) analysis corroborated the elemental composition and purity of the synthesized nZVI-TiO_2-SiO_2 nanocomposites. The EDS spectra reveal a progressive mass ratio of silicon, zero-valent iron (nZVI), and titanium atoms with relatively higher mass ratio of oxygen. Higher mass percentage of titanium with nearly equal mass percentage of silicon and zero valent iron (15.78% and 15.48% mass percent respectively) confirm the existence of the Fe^0 and Si as a coating layer of approximately equal mass percents in the nanocomposite material. Ti mass percents 18.52% exist relatively higher after oxygen (50.22%) in the nanocomposite as the titania (TiO_2) nanoparticles are the "core" material in the nanocomposite. The distribution and relative abundance of the incorporated nanoparticles are governed by interfacial interactions, redox reactions, and particle nucleation and growth dynamics. These fundamental mechanisms are themselves highly dependent on the reaction pH, as established in prior studies.[40,68–70]

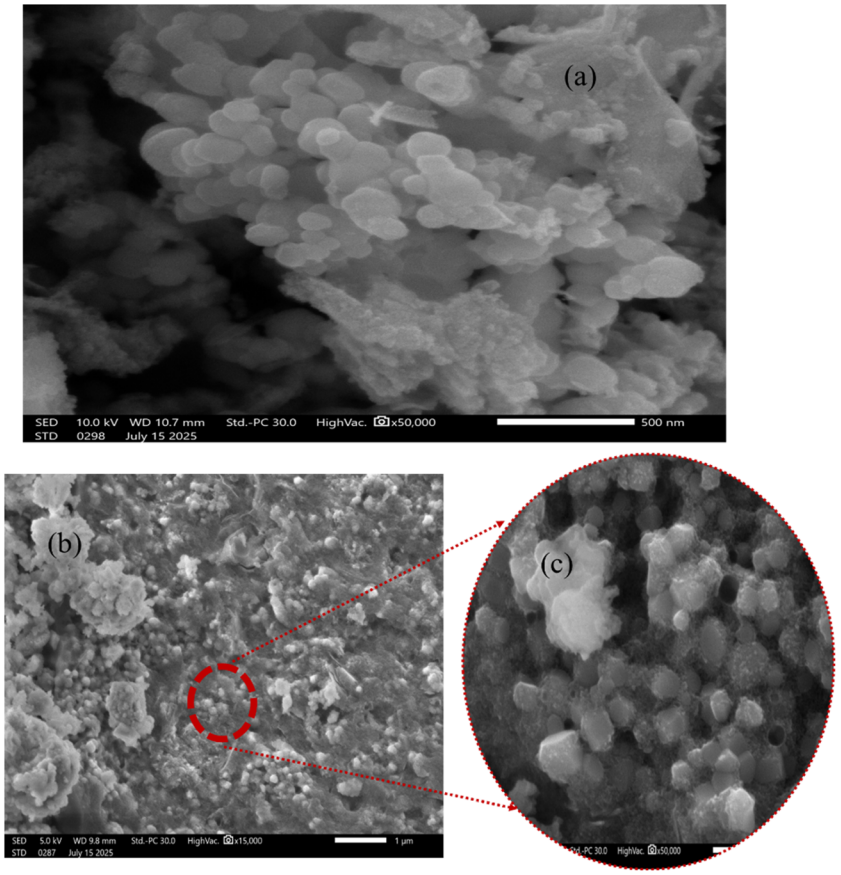

Fig. 2 FESEM analysis of TiO_2-nZVI ×50 000 magnification (a), silica coated TiO_2-nZVI nanoparticles ×15 000 magnification (b) and (c) selected area of silica coated TiO_2-nZVI ×50 000 magnification.

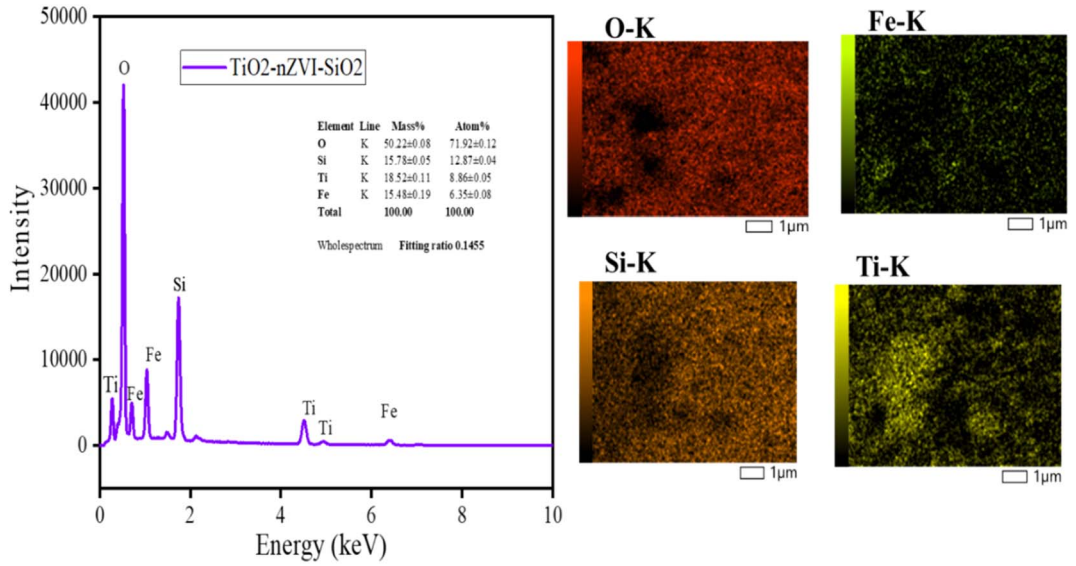

Fig. 3 EDX analysis of silica coated TiO_2-nZVI nanoparticles.

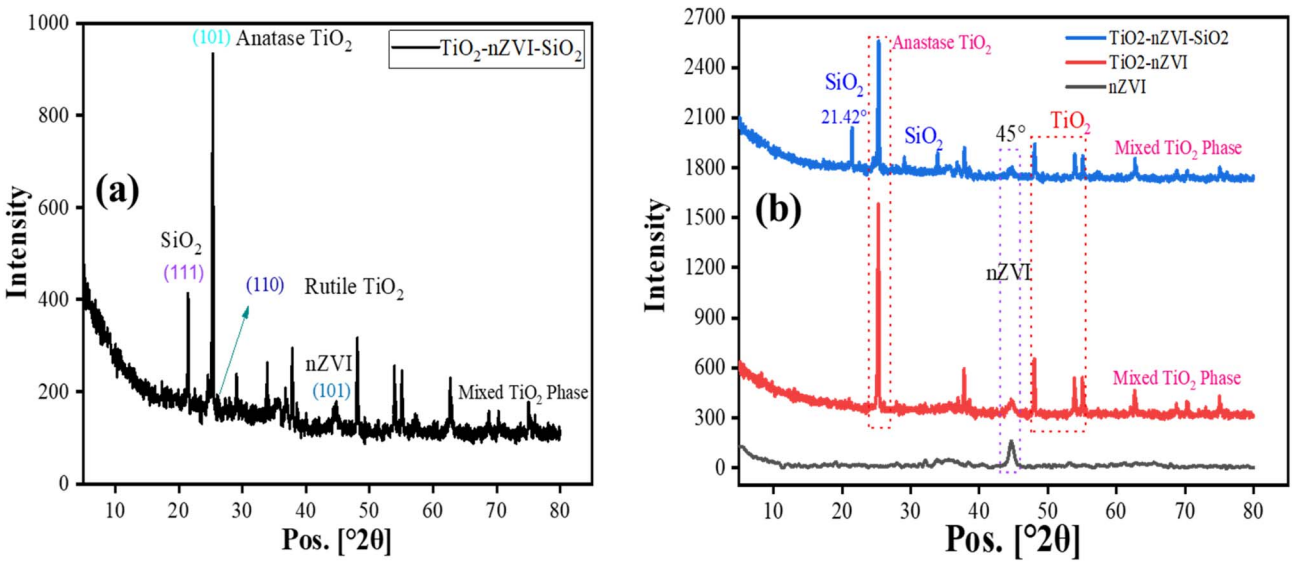

Fig. 4 X-ray diffraction pattern of nZVI, TiO_2-nZVI and TiO_2-nZVI-SiO_2 nanoparticles (a) TiO_2-ZVI-SiO_2 (b) Comparison of diffraction patterns of ZVI, TiO_2-nZVI and TiO_2-nZVI-SiO_2 nanoparticles.

The EDX analysis of the TiO_2-nZVI-SiO_2 nanoparticles confirms the results of the FTIR analysis and a successful synthesis of nZVI-TiO_2-SiO_2 nanocomposite material with the desired elemental composition. The results highlight the effective two-layer coating of nZVI and SiO_2. The uniform distribution of nZVI and silicon highlights the effectiveness of the coating method, which is crucial for maximizing the material's reactivity and stability in environmental applications.

3.3 X-ray diffraction (XRD) analysis of nZVI, TiO_2-nZVI and TiO_2-nZVI-SiO_2 nanocomposite

Fig. 4 shows the crystalline structure and phase composition of the synthesized nZVI, TiO_2-nZVI, TiO_2-nZVI-SiO_2 nanoparticles analyzed using Rigaku SmartLab Powder X-ray Diffractometer. The resulting patterns Fig. 4(a and b) exhibits characteristic peaks of a binary crystalline material coated by an amorphous Silica matrix. The XRD peaks in Fig. 4(a) (see Table 2) corroborates the existence of dominant anatase titanium dioxide, TiO_2 and a metallic zero valent iron, Fe^0.[71–74] The most prominent peak at 25.3° is indexed to the 101 plane[75] of the anatase phase (JCPDS No. 21-1272). This confirmed the presence of the TiO_2 photocatalytic component which forms the core of the synthesized TiO_2-nZVI-SiO_2 nanocomposite and reinforces its overall stability and chemical activity.[76–78] The anatase 37.8° indexed 004 plane, 48.0° indexed 200 plane and a distinct peak corresponding to the 105 plane at 53.9° confirms the high purity of the anatase phase of the TiO_2 component. In addition, there is

Table 2 XRD reflection index of the synthesized TiO_2-nZVI-SiO_2 nanoparticles

Phase	2θ (°)	Crystal plane (*hkl*)	JCPDS card	Ref.
TiO_2 (anatase)	25.3	(101)	21-1272	75
TiO_2 (anatase)	37.8	(004)	21-1272	75
TiO_2 (anatase)	48.0	(200)	21-1272	75
TiO_2 (anatase)	53.9	(105)	21-1272	75
Fe	44.7	(110)	06-0696	79
Fe	65.1	(200)	06-0696	80
Amorphous SiO_2	15–30 (broad hump), 20.2	(111)	00-022-1536	81

nearly complete absence of the main rutile (110) peak at 27.4° (see Fig. 4(a)).

A critical peak of zero-valent iron, magnetic and reductive component of the TiO_2-nZVI-SiO_2 nanocomposite, is observed at 44.7°, indexed (110) JCPDS 06-0696 which is the fingerprint of the nZVI materials.[79] However, a small wide peak at 65.1° indexed to the iron (200) plane is associated with the Fe^0. The peak reflection at 35.4° could be associated with the formation of iron oxide shells such as Fe_3O_4 and γ-Fe_2O_3 which form upon the exposure of Fe^0 to air during XRD analysis. However, these narrow passive layers usually produced *via* surface oxidation often serve to stabilize the highly reactive nZVI core.[82–84] The broad silica hump across approximately 15° to 30°, coupled with the absence of sharp, characteristic peaks of SiO_2 in the form of quartz, revealed that the SiO_2 component exists predominantly in an amorphous state.[85,86] The amorphous SiO_2 acts functionally as an inert and a stabilizer.[63] Hence, it is highly essential for mitigating the intrinsic agglomeration potential of the nZVI and its possible influence on the synthesized TiO_2-nZVI nanocomposite.[58] In addition, amorphous SiO_2 coating bolsters the available surface area of the coated TiO_2-nZVI material for synergistic catalytic and reductive reactions.[81]

3.4 XPS analysis of TiO_2-nZVI-SiO_2 nanocomposite

Fig. 5 illustrates the X-ray photoelectron spectroscopy analysis of the nanocomposite material. The full survey spectrum in Fig. 5(a) confirmed the presence of titanium (Ti), iron (Fe), and silicon (Si) in the synthesized nanocomposite. Fig. 5(b) deconvoluted *via* Gaussian model provides a detailed survey of the chemical and electronic interaction of titanium spectrum (Ti 2p) in the nanocomposite material. The well-defined doublet of the Ti $2p_{3/2}$ and Ti $2p_{1/2}$ peaks were observed at binding energy, BE = 458.7 eV and BE = 464.4 eV respectively. The peaks binding energy separation were found to be BE = 5.7 eV conforming with the predominant +4 oxidation state, Ti^{4+}. The absence of Ti^{3+} suggest a successful integration of TiO_2 with the nZVI.[87] In Fig. 5(c), on the other hand, the characteristic Fe $2p_{3/2}$ and Fe $2p_{1/2}$ spin orbit splitting peaks with two minor peaks located at BE = 705.6 eV and BE = 718.6 eV respectively which are consistent with the XPS findings in ref. 88 and 89. These minor peaks associated with lower intensities are characteristic property of nano zero valent iron, Fe^0.[90] Subsequently, the passivated iron layers Fe $2p_{3/2}$ and Fe $2p_{\frac{1}{2}}$ located at BE = 711 eV and BE = 724.5 eV are a specific characteristic of oxidized Fe^0 iron species (Fe^{2+} and Fe^{3+}) with a potential formation of Fe–OOH and Fe_3O_4 iron oxides,[82,83] confirming the core shell structure of coated nZVI on TiO_2 nanoparticles. Fig. 5(d) depicts the detailed survey region of Si 2p, the deconvolution shows two distinct peaks correlated to bulk SiO_2 and silicon metal interface (Si–O–Metal) located at BE = 103.5 eV and BE = 102.5 eV respectively. The bulk SiO_2 binding energy is consistent with tetrahedral network within the amorphous SiO_2 matrix[91–93] corroborating the XRD findings of the amorphous nature of silica layer (refer to Section 3.4), coating the nanocomposite material. The silicon metal interface will enable strong interfacial interaction of Si–O–x with Fe^0,[63] leading to the formation of Si–O–Fe,[63] while making SiO_2 a strong chemical interface supporting electron coupling in the TiO_2-nZVI-SiO_2 nanocomposite material. In the O 1s spectrum (Fig. 3(b)), a prominent peak at approximately BE = 529 eV corresponds to the lattice oxygen bond in metal oxides (M−O), while a smaller deconvoluted peak at BE = 532.5 eV is attributed to O–H bonds,[94,95] confirming the presence of oxygen atoms associated with surface hydroxyl groups on SiO_2,[96] TiO_2 and Fe–OOH or Fe_2O_3.[4] The detailed region analysis of the C 1s XPS spectra was deconvoluted into four distinct peaks *via* similar Gaussian model (see Fig. 5(f)). The centered peak at BE = 284.8 eV is assigned to C–C and C–H bonds associated with adventitious hydrocarbon contaminants.[97] the peak at BE = 286.0 eV to 287.0 eV and BE = 288.5 eV to 289.5 eV is attributed to oxidized C–O or C–OH and C═O or O–C═O functional groups.[98–101] The presence of these oxidized byproducts could be associated with the exposure of adventitious carbon from residual organic precursors utilized in the nanoparticle synthesis to the atmospheric air. Recalling that the synthesized particles were washed several times with ethanol as described in Section 3. At low-binding energy BE = 283.0–284.0 eV signifies C–Metal bonds, particularly metal carbides such as Ti–C, Fe–C[102] and Ti–Fe–C.[103] However, there was no anatase peak indicating Ti–C bond which is commonly located near 281 eV, suggesting absence of carbon–oxygen replacement in the anatase TiO_2 lattice.[104,105] Consequently, the formation of these metal carbides at low BE signifies a successful chemical interaction between the nZVI with carbon species confirming electronically coupled and stable nanocomposite. These properties are crucial for overall material catalytic activity, functionality and structural integrity. The overall nanocomposite components selection was designed

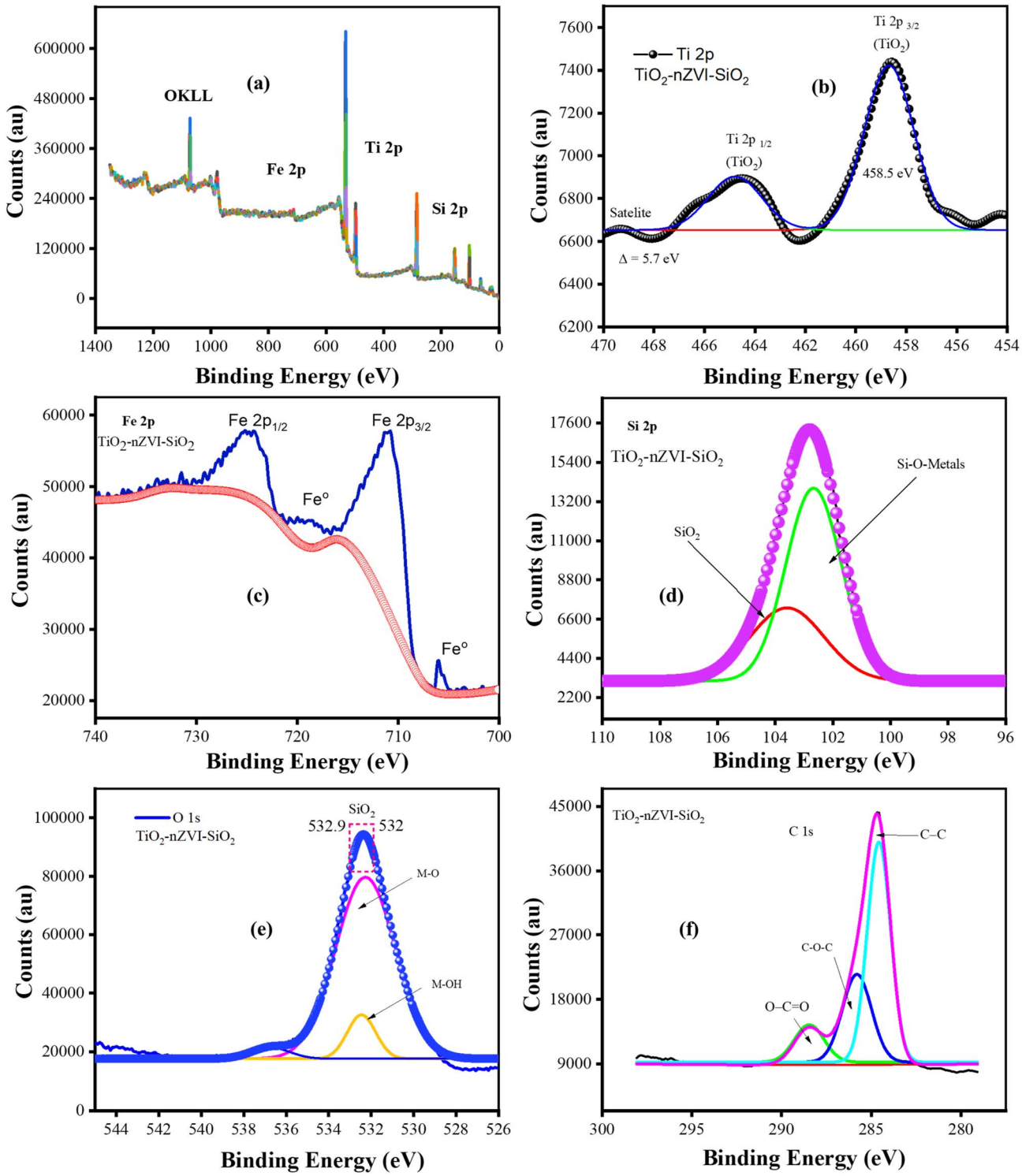

Fig. 5 TiO_2-ZVI-SiO_2 XPS analysis. Full survey response (a), and (b–f) detailed survey of regions Ti 2p, Fe 2p, Si 2p, O 1s, and C 1s.

for synergistic activity, where the TiO_2 shell can facilitate the photocatalytic activity and enhanced electron transfer from the underlying nZVI, a mechanism known to boost contaminant reduction. Furthermore, the SiO_2 matrix not only stabilizes the composite against aggregation but also modulate interfacial electron dynamics as shown in the Si 2p spectral analysis.

3.5 TGA analysis of TiO_2-nZVI-SiO_2 nanocomposite compared with TiO_2-nZVI nanoparticles

Fig. 6 shows the thermal gravimetric analysis of TiO_2-nZVI-SiO_2 and compares the degradation properties with the precursor TiO_2-nZVI composite to evaluate the influence of the SiO_2 layer on the thermal behavior and structural stability. From Fig. 6(a–

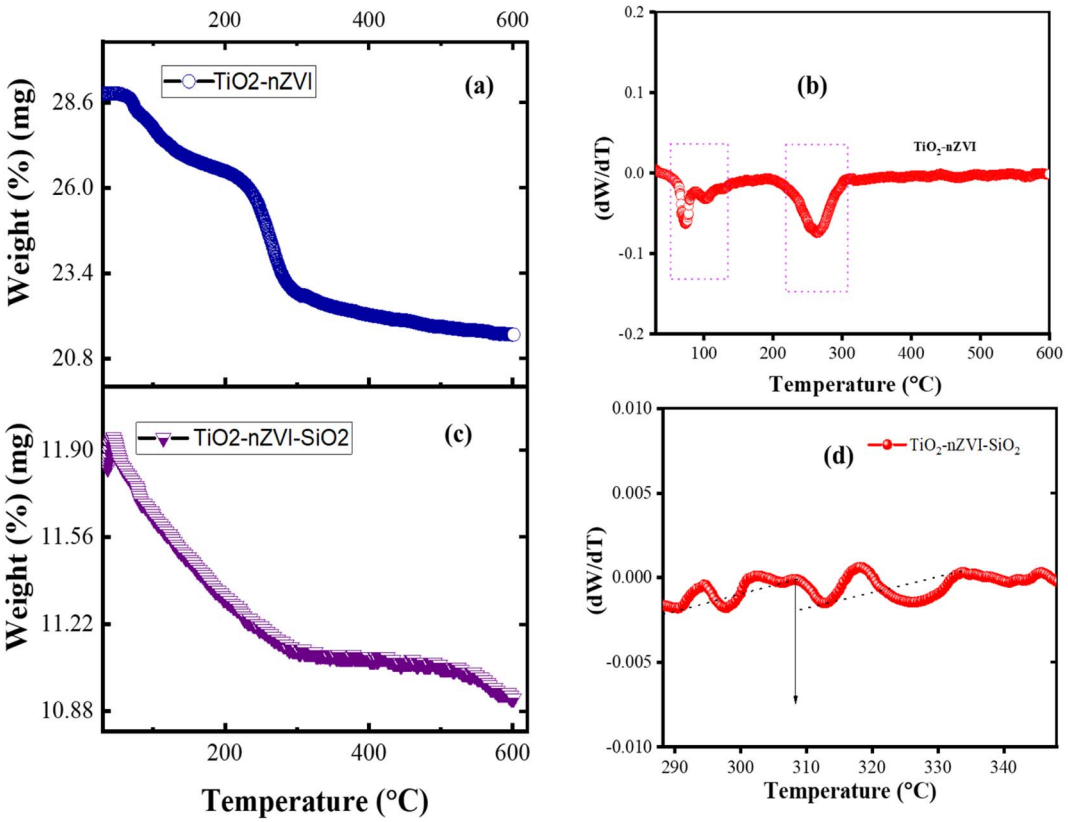

Fig. 6 TGA Analysis of TiO_2-nZVI and TiO_2-nZVI-SiO_2 (a and c), weight 1st order differential of TiO_2-Nzvi and TiO_2-nZVI-SiO_2 (b and d) nanocomposite.

c), the TiO_2-nZVI composite shows multi-stage thermal degradation profile (see S1 TGA 1&2), with a total weight loss of 38 w% across the TGA temperature range. The first degradation stage at 150 °C, characterized by 5 wt% to 8 wt% loss, is attributed to the removal of physiosorbed water and residual solvent molecules.[41,106] Weight loss from 150 °C to 800 °C is associated with the decomposition of organic species, such as –O–H groups on the nanocomposite surface, and the oxidation of the nZVI core to iron oxides such as Fe_3O_4 or Fe_2O_3.[107] The constant degradation of the composite material at this stage implies nearly complete thermal oxidation of the reactive nZVI core and the initial exposure of TiO_2 shell. In (Fig. 7(c)) the TiO-nZVI-SiO_2 composite revealed better thermal stability, with a total mass loss of 3% across the TGA temperature range. The flat TGA curve indicates high thermal stability of the SiO_2-coated nanocomposite material, which is consistent with the findings in ref. 107 where SiO_2 was reported to enhance the thermal stability of TiO_2 in TiO_2–SiO_2 nanocomposite. The SiO_2 layer functions as a protective barrier that restricts the diffusion of oxygen and moisture to the nZVI, slowing the thermal oxidation and overall aggregation of the SiO_2-coated nanocomposite.

3.6 Membrane properties and performance evaluation

3.6.1 X-ray diffraction (XRD) analysis. The XRD analysis was employed to elucidate the crystalline structure and phase composition of TiO_2-nZVI-SiO_2 membranes modified by varying TiO_2-nZVI-SiO_2 loadings, in comparison to an unmodified control membrane (see Fig. 7). The diffractograms for all membranes exhibited prominent peaks at 2θ angles approximately at $2\theta = \sim 18.39°$ associated to α-phase PVDF,[108–110] and $2\theta = 20.22°$ are characteristic of the electroactive β-phase of PVDF, a finding consistent with the previous findings in ref. 111–115. These peaks correspond to reflections from the (110) and (020) crystallographic planes, confirming the β-phase as the thermodynamically dominant crystalline polymorph in the nanocomposite system. The broadening peaks observed at $2\theta = 20.22$ with increasing TiO_2-nZVI-SiO_2 loading could be associated with increase in the amorphous SiO_2 in the polymer matrix.[116] A secondary diffraction peak observed at around $2\theta = \sim 28.5°$ was identified as the (101) plane of the anatase phase of TiO_2.[41,114] However, there is a progressive variation in this peak's intensities observed with increasing TiO_2-nZVI-SiO_2 loading, providing greater density for active sites. Hence, the crystallinity of the membrane increases with increasing nanoparticles loading (see S1 C1–C10) which aligns with previous research findings correlating polymer functionalization with PVDF crystallinity, enhancing functional interactions and molecular ordering within the PVDF polymer matrix ((Jeong *et al.*, 2023) Jeong *et al.*, 2018; Pyo *et al.*, 2024).

3.6.2 FTIR analysis of the PVDF and modified TiO_2-ZVI-SiO_2 nanocomposite membrane. The FTIR analysis of the PVDF and TiO_2-nZVI-SiO_2 modified nanocomposite membranes were

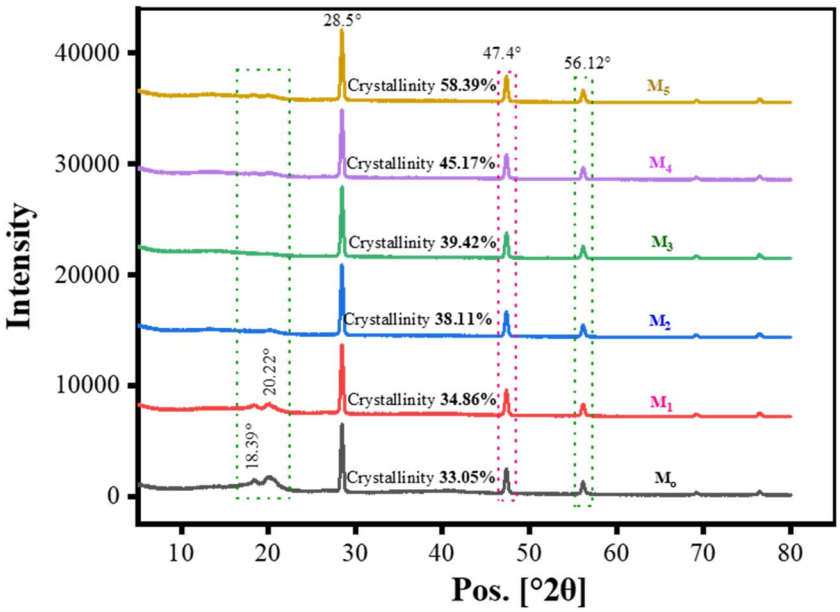

Fig. 7 XRD analysis of PVDF and PVDF incorporated TiO_2-ZVI-SiO_2 nanocomposite membranes at varying nanocomposite loading (Mo = pristine PVDF; M1 = 0.1 g, M2 = 0.15 g, M3 = 0.20 g, M4 = 0.25 g and M5 = 0.3 g TiO_2-ZVI-SiO_2).

conducted (see Fig. 8) to support further analysis on the incorporation of TiO_2-nZVI-SiO nanocomposite and determine the interactions between the nanoparticles and membrane functional groups as well as the structural modifications of PVDF and the modified nanocomposite membranes. The spectra of the samples *viz.* Mo, M1, M2, M3, M4, and M5 are moderately congruent, indicating that the incorporation of TiO_2-nZVI-SiO_2 nanocomposite slightly alters the fundamental chemical functionalities of the PVDF polymer. As the TiO_2-nZVI-SiO_2 loading increases there appears an overall increase in intensities in the modified nanocomposite membranes. This is evidenced by observing the characteristic peaks of the PVDF matrix in the Mo to M5 samples *viz.* CH_2 wagging at 1400 cm^{-1}, CF_2 asymmetrical stretching at 1176 cm^{-1}, C–C asymmetrical stretching at 876 cm^{-1}, and a combined peak at 840 cm^{-1} for CF_2 stretching and CH_2 rocking. The typical –OH stretching vibration expected between 3300–3600 cm^{-1},[57,110] was observed at 3500 cm^{-1}. Two additional moderate deviation from Mo was

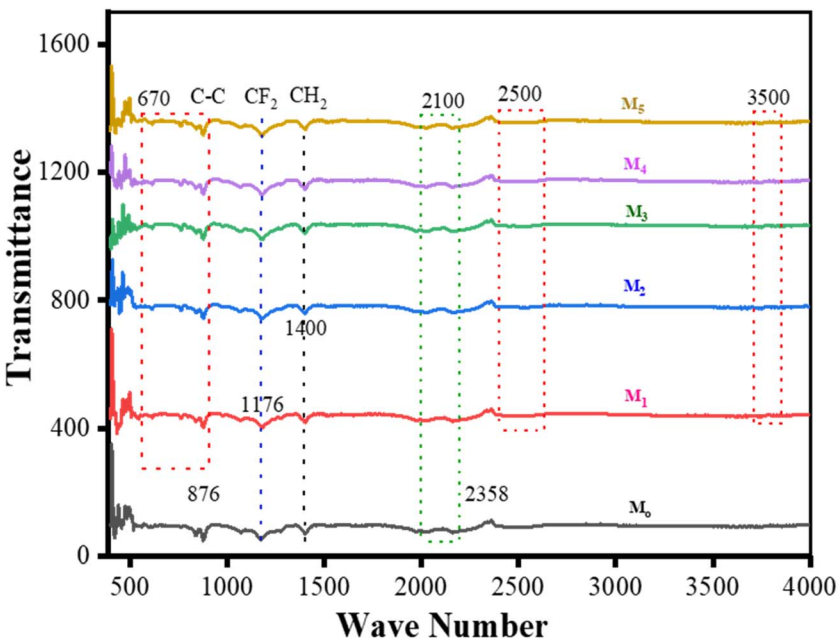

Fig. 8 FTIR analysis of PVDF and TiO_2-nZVI-SiO_2 modified nanocomposite membranes (Mo = pristine PVDF; M1 = 0.1 g, M2 = 0.15 g, M3 = 0.20 g, M4 = 0.25 g and M5 = 0.3 g TiO_2-ZVI-SiO2).

Table 3 Surface and cross-sectional morphologies of the PVDF incorporated TiO_2-nZVI-SiO_2 nanocomposite membranes

Nanocomposite membrane composition	Surface morphology	Cross sectional morphology
Mo-pristin @PVDF	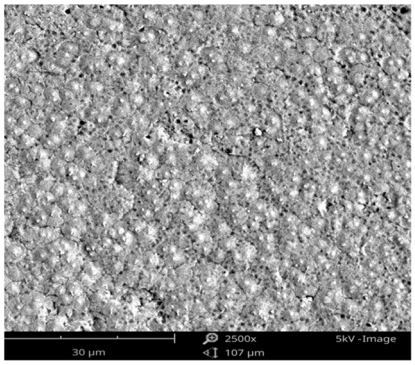	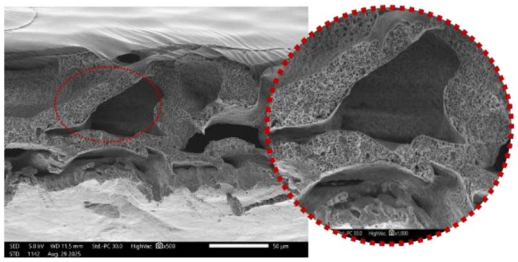
M1-0.10 g @ TiO_2-nZVI-SiO_2	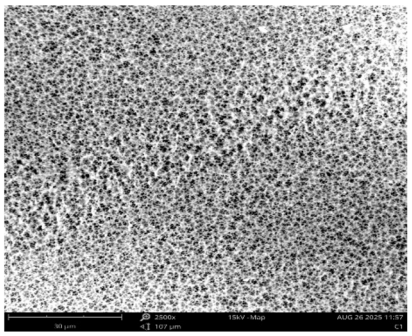	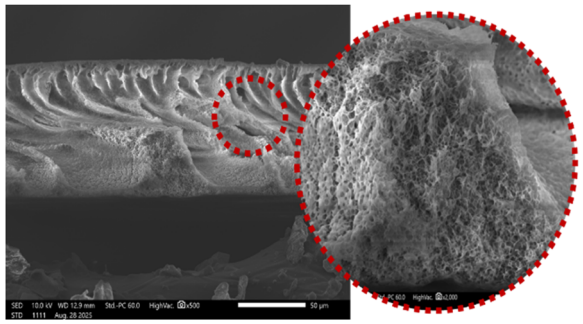
M2-0.15 g @ TiO_2-nZVI-SiO_2	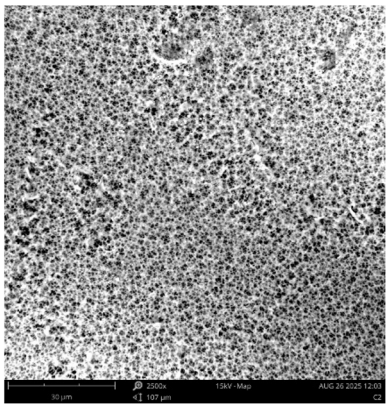	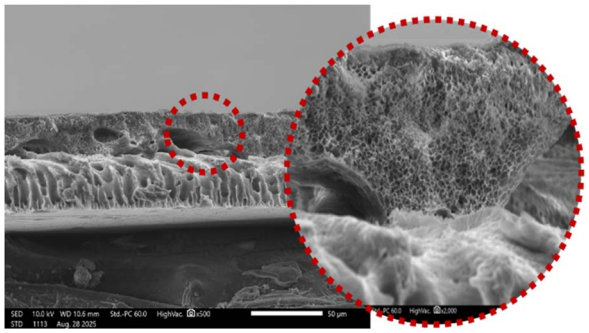
M3-0.20 g @ TiO_2-nZVI-SiO_2	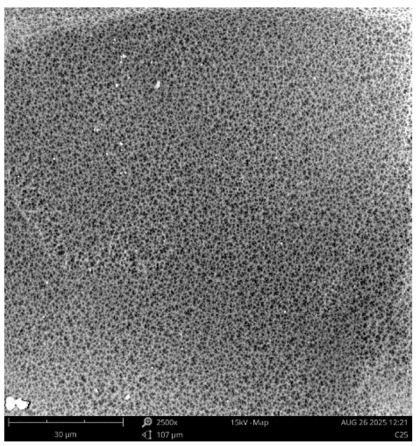	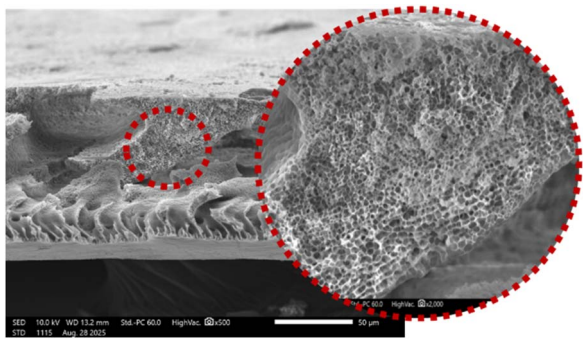

Table 3 (*Contd.*)

Nanocomposite membrane composition	Surface morphology	Cross sectional morphology
M4-0.25 g @ TiO_2-nZVI-SiO_2	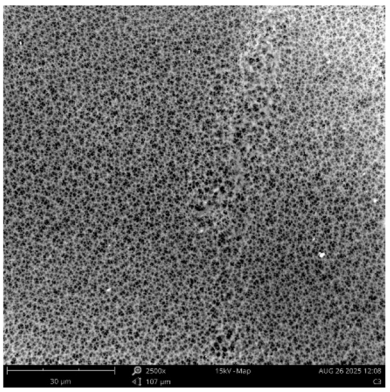	
M5-0.30 g @ TiO_2-nZVI-SiO_2	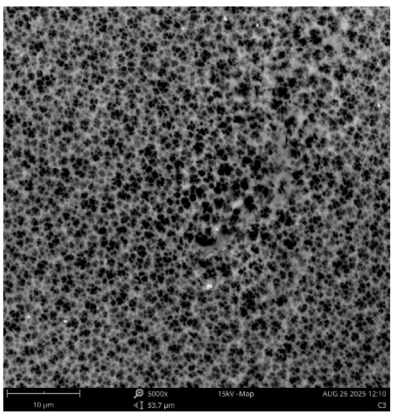	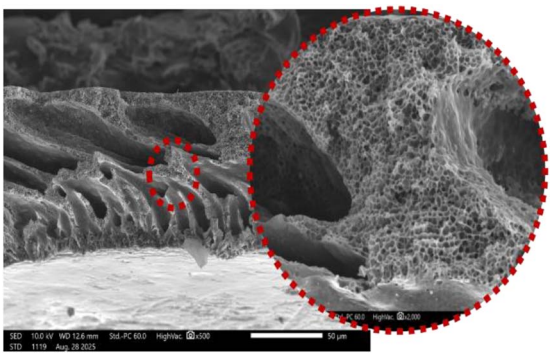

observed on the modified membranes between 670 cm^{-1}, to 876 cm^{-1} C–C vibrations, potentially attributable to specific molecular rearrangement as TiO_2-nZVI-SiO_2 nanocomposite introduced in the PVDF membrane matrix, corroborating the XRD findings on the possible formation of metal carbide Ti–Fe–C[103] and metal oxide such as Ti–O, Fe–O–, Si–O–Si around 1250 cm^{-1}.[119] Where peaks broaden as TiO_2-nZVI-SiO_2 nanocomposite loading increases. The peaks at 740 to 820 cm^{-1}, and 950 cm^{-1} and 960 cm^{-1} revealed consistent increase in hydrophilic functional groups, Si–O–H, Ti–O–H or Si–O–Ti vibrations,[42] further confirming the incorporation of TiO_2 and SiO_2.[120,121] The peak around 500 cm^{-1} is attributed to Fe–O overlapping Ti–O stretching vibrations in the crystalline phases of PVDF nanocomposite matrix.[117,118]

3.6.3 Surface and cross-sectional morphological analysis of the PVDF and modified TiO_2-ZVI-SiO_2 nanocomposite membranes. The surface and cross-sectional morphologies of the modified and unmodified membranes were investigated *via* FESEM and EDX analyses. Based on the FESEM analysis and EDX elemental mapping presented in Table 3 and Fig. 9 respectively, the dispersion of the TiO_2-nZVI-SiO_2 nanoparticles within the PVDF membrane matrix was found to be consistent and significantly influenced by the presence of SiO_2 coating on TiO_2-nZVI nanocomposite material. Since titania TiO_2 and nZVI nanoparticles often exhibit homogeneous dispersion at relatively small loading (0.1 g to 0.15 g) when incorporated in PVDF membranes, as pronounced agglomeration at higher loading are reported in previous studies associated with both TiO_2 and nZVI nanocomposite membranes.[122,123] The morphological homogeneity observed is corroborated by EDX line-scanning of the membrane cross-sections (see Table 3), which revealed a uniform distribution profile across all the TiO_2-nZVI-SiO_2 nanocomposite membranes as opposed to the findings reported by ref. 54 with highly irregular profile for the Si element which were concurrently introduced with TiO_2, contrary to the surface coating approach reported in this study. The agglomeration of nanoparticles is a phenomenon primarily driven by strong interparticle forces such as electrostatic, steric, and van der Waals interactions.[124,125] The incorporation of SiO_2 as a surface layer enhances the nanocomposite homogeneous dispersion, resulting in a uniform particle distribution. The

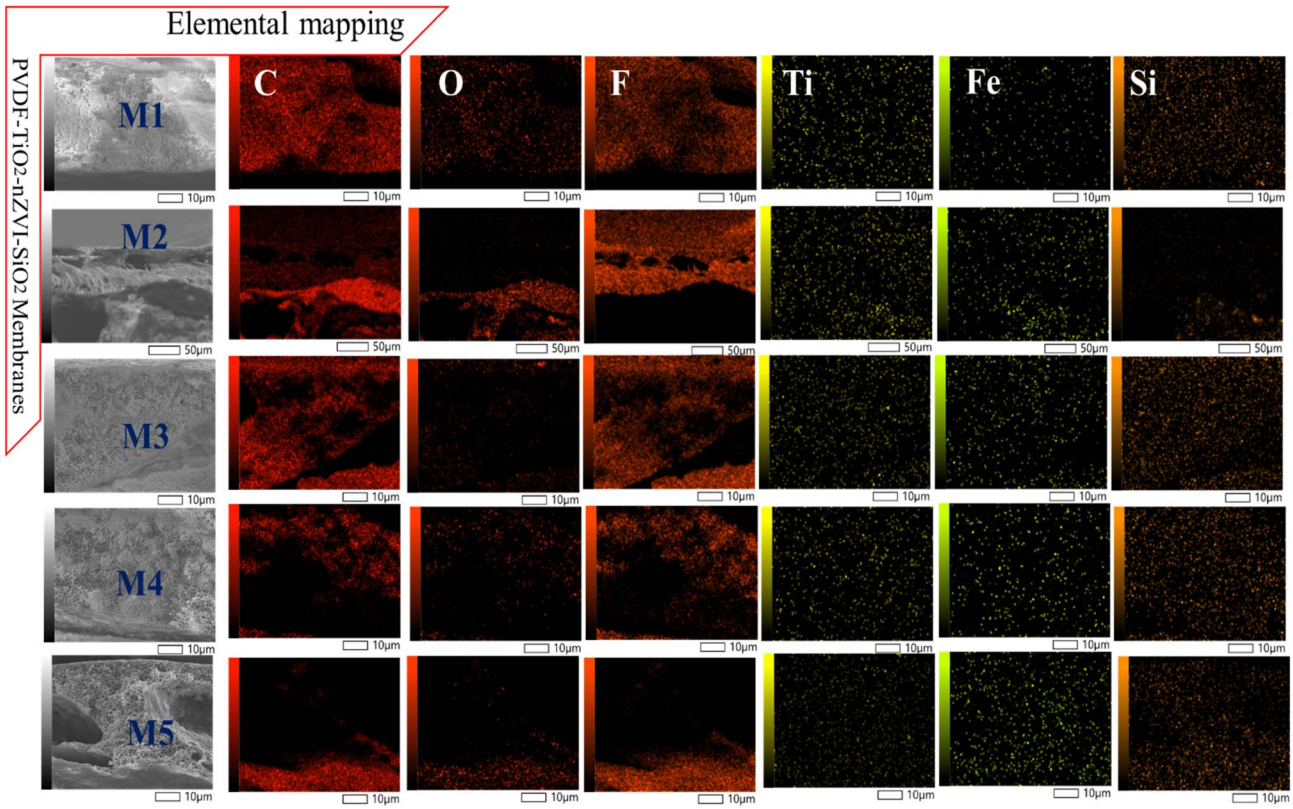

Fig. 9 Elemental mapping of PVDF TiO_2-nZVI-SiO_2 PVDF nanocomposite membrane *via* FESEM/EDX analyses (Mo = pristine PVDF; M1 = 0.1 g, M2 = 0.15 g, M3 = 0.20 g, M4 = 0.25 g and M5 = 0.3 g TiO_2-nZVI-SiO_2).

EDX analysis confirmed the presence of SiO_2, TiO_2 and nZVI across all the membrane cross sections.

The results from the FESEM analyses (refer to Table 3) further corroborates the incorporation of TiO_2-nZVI-SiO_2 nanoparticles in the PVDF matrix, as observed by the induced concentration-dependent morphology associated with the presence of titania particles. Consequently, at lower TiO_2-nZVI-SiO_2 loadings 0.10 g to 0.20 g, the nanocomposite exhibited a refined surface pore structure with increased mean pore size while maintaining consistent membrane porosity.[123,126,127] Results from this cross-sectional morphology corroborate the influence of nanocomposite loadings in the formation of extended macro-voids in the membrane structure.[49,128,129] These morphological properties are associated to the TiO_2-nZVI-SiO_2 ability in enhancing the phase inversion process while promoting instantaneous de-mixing and solvent to nonsolvent exchange kinetics. Similarly, higher TiO_2-nZVI-SiO_2 loadings (0.25 g to 0.30 g) instigate a proportional morphological transition. The increased dope solution viscosity delays phase separation, leading to looser sub-layer, more prominent surface pores, and increased overall porosity to 87.53% (see Table 4). This shift, governed by thermodynamic characteristics, results in a structure characterized by higher porosity and a thinner selective layer, which in turn could enhance water permeability.[130,131] However, it could also compromise rejection performance due to the less compact morphology. Table 4 shows characteristics of fabricated nanocomposite membrane.

3.6.4 Hydrophilicity, solvent content and shrinkage ratio analysis of the nanocomposite membrane. The porosity trend shown in Table 4 are a result of thermodynamic influence governing the structural configuration and hydrophilic nature of the PVDF nanocomposite membrane during phase inversion. These thermodynamic parameters are shown to significantly influence a consistent non-solvent to solvent interaction at 0.1 g

Table 4 Characteristic properties of the PVDF TiO_2-nZVI-SiO_2 incorporated nanocomposite membranes

Modified membrane	Average membrane thickness (μm)	Membrane pore size × 10^{-3} (μm)	Membrane porosity (%)	Crystallinity (%)
0.10 g TiO_2-nZVi-SiO_2	49	11.874	83.81	34.86
0.15 g TiO_2-nZVi-SiO_2	53	11.836	85.30	38.11
0.20 g TiO_2-nZVi-SiO_2	55	11.747	85.90	39.42
0.25 g TiO_2-nZVi-SiO_2	56	11.770	85.92	45.17
0.30 g TiO_2-nZVi-SiO_2	58	11.746	87.53	58.39

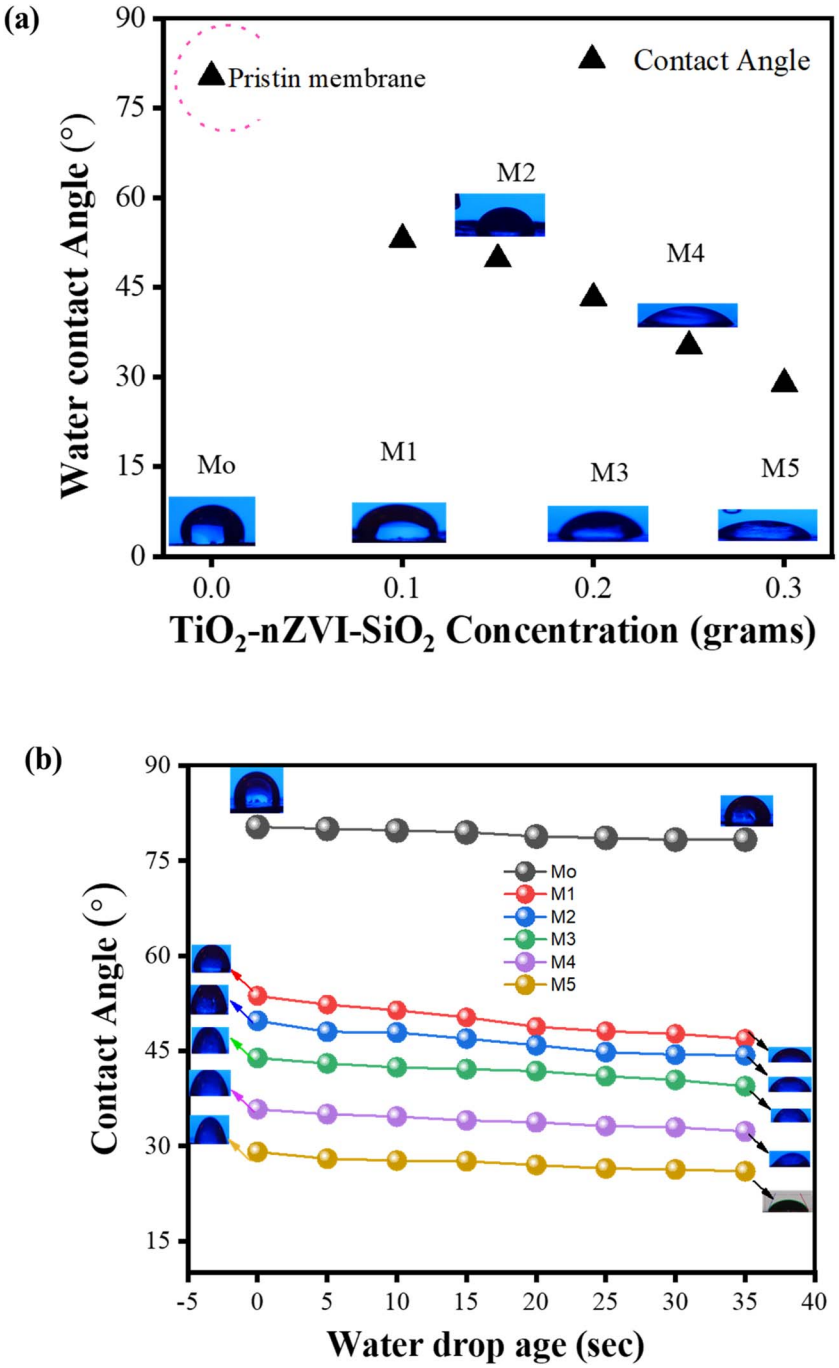

Fig. 10 (a) Hydrophilicity assessment *via* membrane water contact angle analysis of PVDF and TiO_2-nZVI-SiO_2 modified nanocomposite membranes (Mo = pristine PVDF; M1 = 0.1 g, M2 = 0.15 g, M3 = 0.20 g, M4 = 0.25 g and M5 = 0.3 g TiO_2-ZVI-SiO_2). (b) Time dependent contact angle measurement analysis of PVDF and TiO_2-nZVI-SiO_2 modified nanocomposite membranes (Mo = pristine PVDF; M1 = 0.1 g, M2 = 0.15 g, M3 = 0.20 g, M4 = 0.25 g and M5 = 0.3 g TiO_2-ZVI-SiO_2).

to 0.15 g and 0.2 g to 0.3 g TiO_2-nZVI-SiO_2 nanocomposite loadings yielding membrane with relatively consistent pores sizes and overall porosity. Hydrophilicity is the ability of the membrane to interact with polar solvents such as water, ethanol or acetone and assessed *via* contact angle analysis. Hydrophilic property is significantly imperative in membrane technology, particularly for membrane materials developed for environmental remediation and water purification technologies.[132,133] Fig. 10(a) shows the results of water contact angle analysis conducted using contact angle goniometer at various locations on the membrane samples. From this figure, the water contact angle, a major surface wettability, of the nanocomposite membrane, is shown to be inversely proportional to the increase in nanocomposite loading, implying an increase in affinity to polar solvents with corresponding increase in nanocomposite loading which conforms with the results of XRD, SEM and the

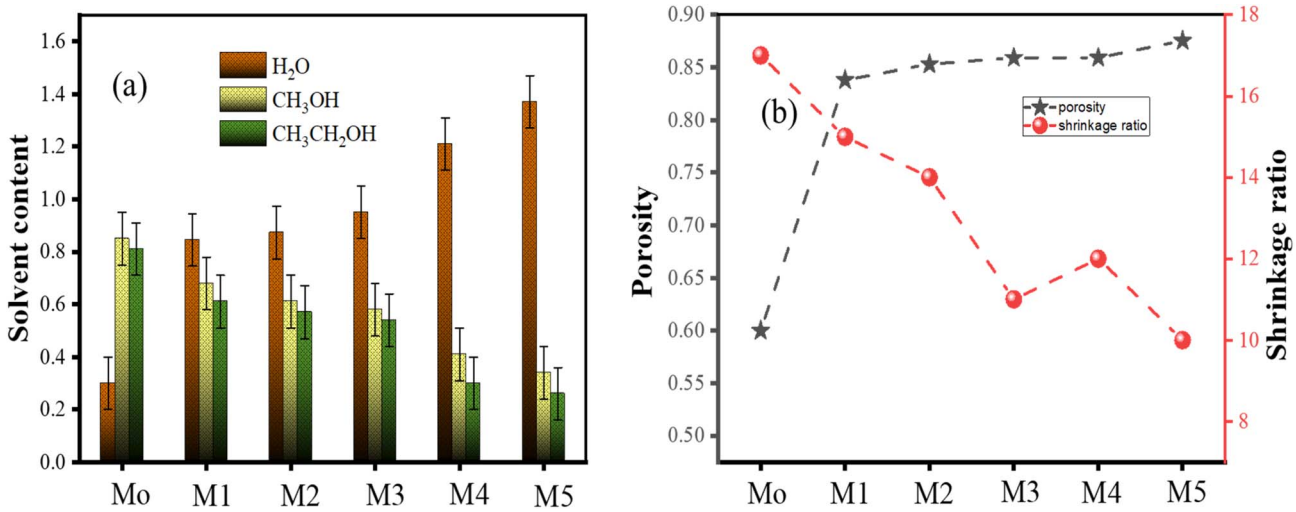

Fig. 11 Solvent content (a), porosity and % shrinkage ratio (b), analysis of PVDF and TiO_2-nZVI-SiO_2 modified nanocomposite membranes (Mo = pristine PVDF; M1 = 0.1 g, M2 = 0.15 g, M3 = 0.20 g, M4 = 0.25 g and M5 = 0.3 g TiO_2-ZVI-SiO_2).

membrane characteristics highlighted in Table 3. The contact angle decreases from pristine PVDF 80.29° to 53.07°after 0.1 g loading of the TiO_2-nZVI-SiO_2 nanocomposite. Subsequently the hydrophilicity continues to increase with increase in TiO_2-nZVI-SiO_2 nanocomposite concentration recording contact angle of 49.76° and 43.26° at 0.15 g and 0.20 g TiO_2-nZVI-SiO_2 respectively. The optimum value of 28.86° was attained at 0.30 g nanocomposite concentration (see Fig. 10(a)). This continuous decline in water contact angle corroborated an enhanced hydrophilic property of the hydrophobic PVDF surface due to modification of the membrane surface matrix by the synergistic effects of metallic nZVI[133] and incorporation of additional active sites of the hybrid TiO_2-nZVI-SiO_2 nanoparticles. Influence of de-mixing on the membrane porosity and hydrophilicity observed was highly insignificant contrary to the previous findings reporting nZVI and Silane effects in the SiO_2 nanocomposite membranes.[133,134] However, water contact angle of membrane materials constantly changes as the water drop ages, making their measurements significantly time dependent. Fig. 10(b) shows the time dependent water contact angle analysis conducted after every 5 seconds. The results confirmed that the presence of TiO_2-nZVI-SiO_2 in the membrane matrix significantly reduces the age of water drop on the membrane surface, as the water drop is being absorbed by the membrane. Consequently, this reduces water drop volume and the total contact angle.[135] These findings confirm the initial membrane properties and the trend observed in Fig. 10(a), it further provides insights into the flux performance of the fabricated membrane.

Fig. 11 shows the results from solvent content analysis (11a) and the relationship between membrane porosity and membrane shrinkage ratio (11b). The solvent content of the nanocomposite membrane was evaluated using water, methanol and ethanol with the relationship described in eqn (8). The results from this analysis revealed a proportional relation of H_2O content with membrane porosity and hydrophilicity conforming the findings in ref. 43. A significant decline in the trend, from 0.78 to 0.11, was observed across the modified nanocomposite membranes (M1 to M5). This decline corresponds to a decreased solvent polarity, as demonstrated by the ethanol and methanol solvents shown in Fig. 11a. To further evaluate this membrane characteristic property and its relationship with membrane porosity, membrane percent shrinkage ratio was computed following eqn (9) and compared with the membrane porosity,[136] see Fig. 11b. Consistent with prior research, the findings establish an inverse correlation between membrane porosity and the shrinkage ratio.[137] The modified membrane, M5 with the maximum porosity and nanocomposite loading showed minimum shrinkage ratio corroborating its suitability for purification technology.

3.6.5 Pure water flux and heavy metal removal analysis of the nanocomposite membrane. The results from the pure water flux analysis are shown in Fig. 12. The Pristine PVDF membrane attained steady flux values after 25 minutes of filtration which was quite faster in relation to the modified TiO_2-nZVI-SiO_2 nanocomposite membrane which stabilizes at varying filtration time as the nanocomposite loading increases across the membrane material, with 40 min for 0.1 g (M1), 45 minutes for 0.15 g (M2) 50 minutes for 0.20 g and 0.25 g (M3 and M4) and about 55 minutes for 0.3 g (M5) nanocomposite membrane respectively. Despite these variations in steady flux filtration time, the minimum steady flux volume increases with increased nanocomposite loading from 70.63545 L m^{-2} h^{-1}, 36.1204 L m^{-2} h^{-1}, 24.88294 L m^{-2} h^{-1} 18.46154 L m^{-2} h^{-1} 13.84615 L m^{-2} h^{-1} to 6.02007 L m^{-2} h^{-1} for the M5, M4, M3, M2, M1, and Mo respectively. The corresponding maximum pure water flux obtained for the corresponding membranes are 563.47826 L m^{-2} h^{-1}, 417.3913 L m^{-2} h^{-1}, 271.30435 L m^{-2} h^{-1}, 219.13043 L m^{-2} h^{-1}, 161.73913 L m^{-2} h^{-1}, and 109.56522 L m^{-2} h^{-1} for M5, M4, M3, M2, M1 and Mo respectively. High flux performance from this analysis which ascends with increasing nanocomposite loading are associated with decreased contact

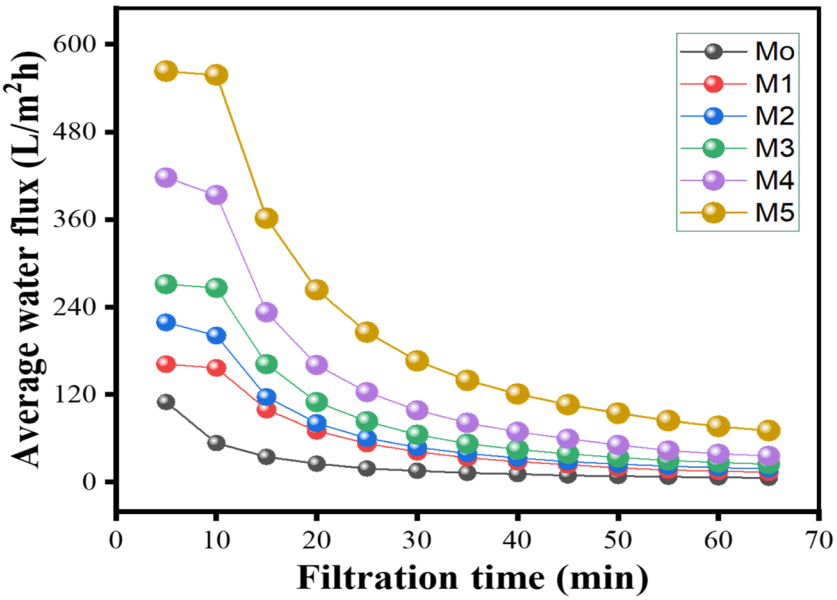

Fig. 12 Pure water analysis of PVDF and TiO_2-nZVI-SiO_2 modified nanocomposite membranes (Mo = pristine PVDF; M1 = 0.1 g, M2 = 0.15 g, M3 = 0.20 g, M4 = 0.25 g and M5 = 0.3 g TiO_2-ZVI-SiO_2).

angle translating to significantly enhanced membrane hydrophilicity. These findings are consistent with the hydrophilicity studies by ref. 52 and 138, solvent content analysis[139] and the reported influence of hydrophilic properties on flux performance.[139,140] Other factors that could influence pure water flux performance apart from hydrophilicity are the membrane thickness, homogeneous interconnected pore network and the potentiality to agglomeration of membrane surface modification materials.[141–143] However, membrane hydrophilic property remains an important parameter in the assessment of flux and anti-fouling performance of nanocomposite membrane for wide industrial applications including water and emulsion separation.[144] In addition, results from the morphological investigation, FESEM and membrane characteristics (see Table 3) show consistent morphological structure and membrane thickness confirming the limited influence of these parameters on the observed overall flux performance of the nanocomposite membranes.

To evaluate the overall performance of the membrane material and determine the optimum nanocomposite loading,

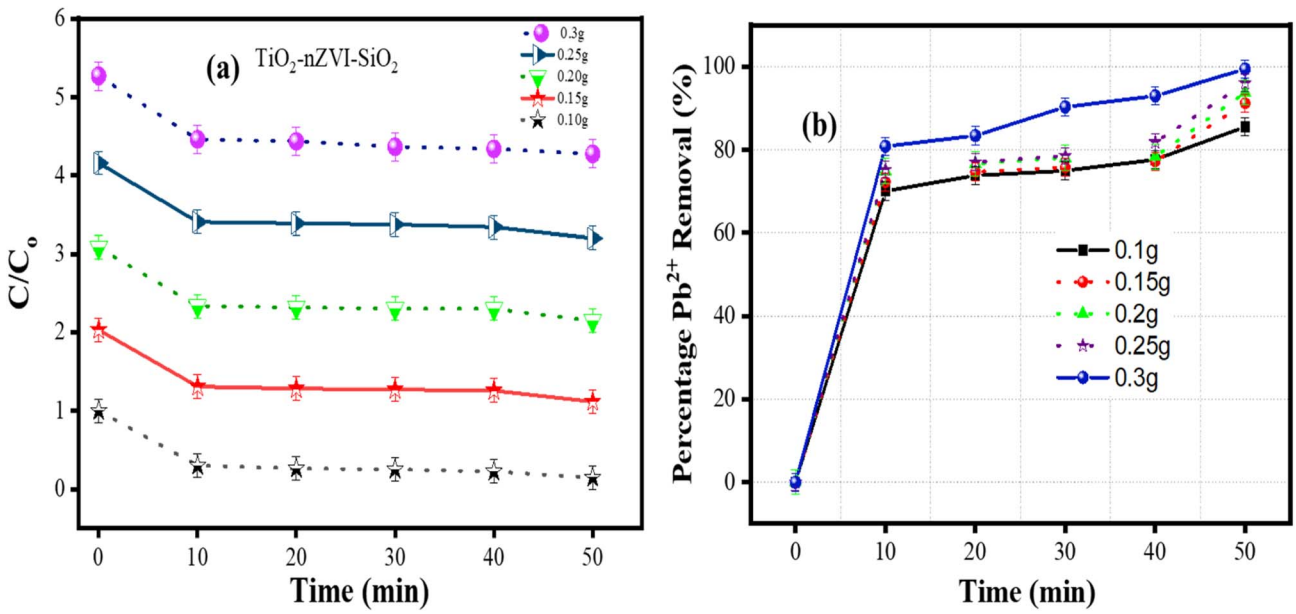

Fig. 13 Concentration gradient (a) and percentage lead removal (b) analysis of TiO_2-nZVI-SiO_2 modified nanocomposite membranes (Mo = pristine PVDF; M1 = 0.1 g, M2 = 0.15 g, M3 = 0.20 g, M4 = 0.25 g and M5 = 0.3 g TiO_2-ZVI-SiO_2).

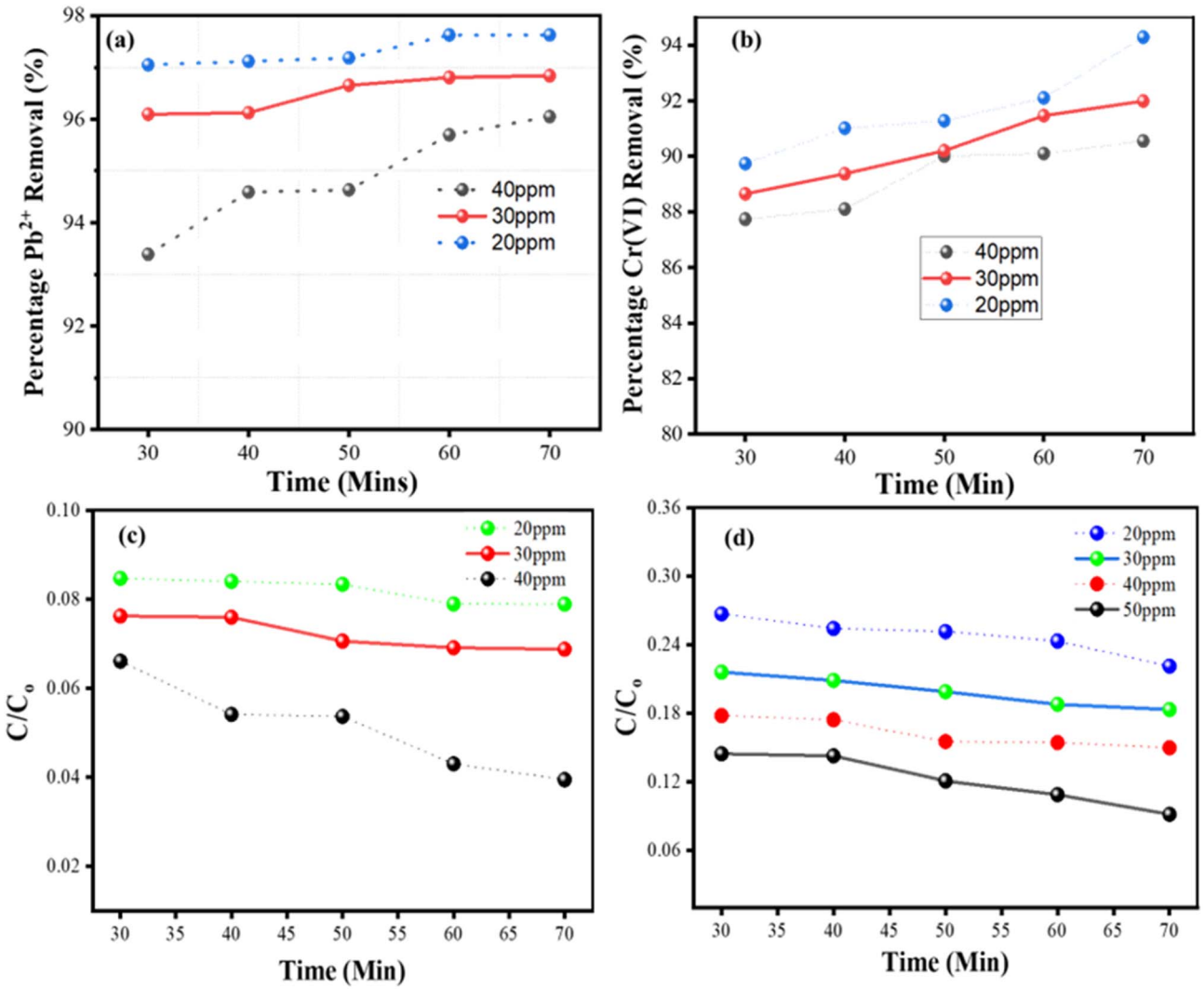

Fig. 14 Influence of heavy metal type and contaminant loading on optimal membrane (M5) performance. (a) Pb^{2+} (20 ppm, 30 ppm, and 40 ppm) and (b) Cr(VI) with corresponding concentration gradients (c and d).

an initial 10 ppm concentration of lead (Pb^{2+}) solution was utilized. The results of filtration experiments obtained for the modified nanocomposite membranes are shown in Fig. 13(a and b). From Fig. 13(a) the concentration gradient shows a sharp decline across all the membranes. The initial rapid decline suggests the impact of combined mechanisms of surface adsorption and size exclusion following redox reaction during the filtration operation,[145] a steady state Pb^{2+} removal rate was subsequently established, confirming the long-term stability of the nanocomposite membranes. The removal efficiencies shown in Fig. 13(b) were found to be proportional to the nanocomposite loading with optimum membrane (M5) achieving 99.8% removal efficiency during the 50 minutes filtration operations. This excellent performance can be associated with an increased number of reactive sites at higher loading of the nanocomposite materials as more of the nZVI and TiO_2 nanoparticles are introduced into the membrane matrix, providing synergistic Pb^{2+} reduction and adsorption capabilities on the modified membrane surface. Namakka *et al.*, (2024) reported similar synergistic behavior of nZVI, TiO_2 and SiO_2 recording 99.9% methylene blue dye removal.[40] Similar mechanisms were reported for chromium(VI)[123] and chlorophenol[146] removal using nZVI-TiO_2 nanocomposite membranes. The enhanced adsorption and reduction capabilities of the developed nZVI-TiO_2 components facilitate the production of reduced lead Pb^{2+} species which are subsequently retained by the modified membrane matrix. While SiO_2 coating, in addition to stabilizing nZVI-TiO_2 and preventing aggregation, ensures effective dispersion and maximum available reactive sites. The optimum membrane (M5) was further utilized in assessing the membrane stability and to investigate the influence of heavy metal types and concentrations by varying concentration of Pb^{2+} and chromium(VI) solutions. The results are shown in Fig. 14(a–d).

The results in Fig. 14(a and b) show the performance of the M5 nanocomposite membrane under 70 minutes of filtration time at 1 bar pressure. The concentration of the tank solutions was varied across the heavy metal filtration solutions: 20 ppm,

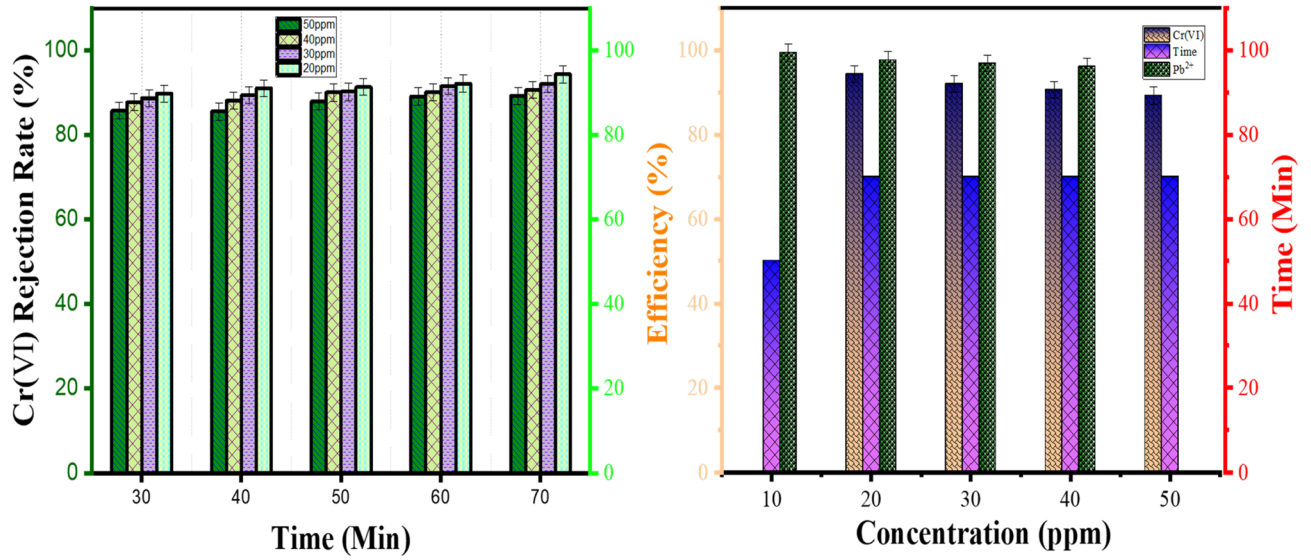

Fig. 15 Comparison of (a) Cr(VI) rejection rate (%) at 20 pm, 30 ppm, 40 ppm and 50 ppm of the optimal membrane (M5) with (b) the overall membrane efficiency over the filtration time.

30 ppm, and 40 ppm for both Pb^{2+} and Cr(VI). Subsequently, the concentration of Cr(VI) was increased to 50 ppm to further explore the membrane boundaries and evaluate overall membrane stability, see Fig. 14(c).

The results revealed maximum removal efficiencies at lower Pb^{2+} and Cr(VI) loadings, which decline as contaminants concentrations increase (refer to Fig. 14(a)). The maximum efficiencies 97.7%, 96.9%, and 96% for 20 ppm, 30 ppm, and 40 ppm Pb^{2+} respectively. Similar trends were observed in Cr(VI) removal experiment (refer to Fig. 14(b)), in which 94.3%, 92%, and ~90% were obtained for 20 ppm, 30 ppm, and 40 ppm, respectively. The trends confirmed the concentration-dependent behaviour of the nanocomposite membrane, which conforms with the findings in ref. 147 and 148. Lower removal rate observed (refer to Fig. 14a and b) with increasing heavy metal loading suggests high concentration of Pb^{2+} and Cr(VI) ions on the reactive sites of the membrane matrix, limiting the kinetic rate of the reduction reaction.[149,150] The plateau at low efficiencies corresponding to higher metal ion loadings (30 ppm and 40 ppm) can be associated with the possible active site's saturation causing overall mass transfer resistance through the nanocomposite membrane.[149] Although the 40 ppm curves show relatively higher removal efficiency (96.9%) in the removal of Pb^{2+} in contrast to the 90% obtained for Cr(VI), the nanocomposite membrane proved to be highly efficient for both Pb^{2+} and Cr(VI) remediation applications. It is imperative to note that the mechanism involved in contaminants removal depends on the nature of the contaminants in addition to the catalytic activity of the nanocomposite membrane. For example, the disparity in the removal efficiencies observed in Pb^{2+} and Cr(VI) can be strongly influenced by the reaction mechanism involved. Since Pb^{2+} cations are easily reduced *via* chemical reduction into metallic lead or converted to Pb $(OH)_2$ or oxyhydroxide, which can be easily retained by the nanocomposite membrane matrix. However, the Cr(VI) reduction mechanisms involve the initial generation of Cr^{3+} species by redox reaction with nZVI components of the nanocomposite membrane followed by subsequent precipitation or adsorption by the TiO_2–SiO_2 components. The synergistic mechanisms of every nanocomposite component allow for efficient removal of these contaminants (>90%).

To further confirm the adsorption behavior of these contaminants onto the PVDF-TiO_2-nZVI-SiO_2 nanocomposite membranes and their interaction with TiO_2-nZVI-SiO_2 particles active sites, equilibrium adsorption isotherm analysis was performed at 25 °C following the procedure described by ref. 114. M1 to M5 membrane data were analyzed using the pseudo first order (PFO), and pseudo second order (PSO) kinetic models. Subsequently the optimal membrane (M5) was subjected to adsorption isotherm analysis using Langmuir isotherms, and the parameters are detailed in S2. Both PSO, PFO and Langmuir model demonstrated a sufficient fit with a higher linear correlation coefficient R^2 ranging from 0.96 to 0.99. The R^2 values (refer to S2) for the PFO and PSO kinetic models corroborate a strong correlation between the experimental data for Pb^{2+} removal and the respective kinetic models, confirming how these models accurately described the adsorption rate.[151] The higher R^2 value of M5 observed (>0.99) for the PSO model suggests chemisorption as the rate limiting step of the adsorption process,[152] in which Pb^{2+} ions are removed by chemical interactions, such as the sharing or exchange of electrons between the Pb^{2+} ions and the hydroxyl functional groups present on the surface of the optimal PVDF-TiO_2-nZVI-SiO_2 nanocomposite membrane, confirming the chemical nature of the binding mechanism, which is characteristic of highly efficient, functionalized adsorbent. Similar findings were reported in previous studies.[114]

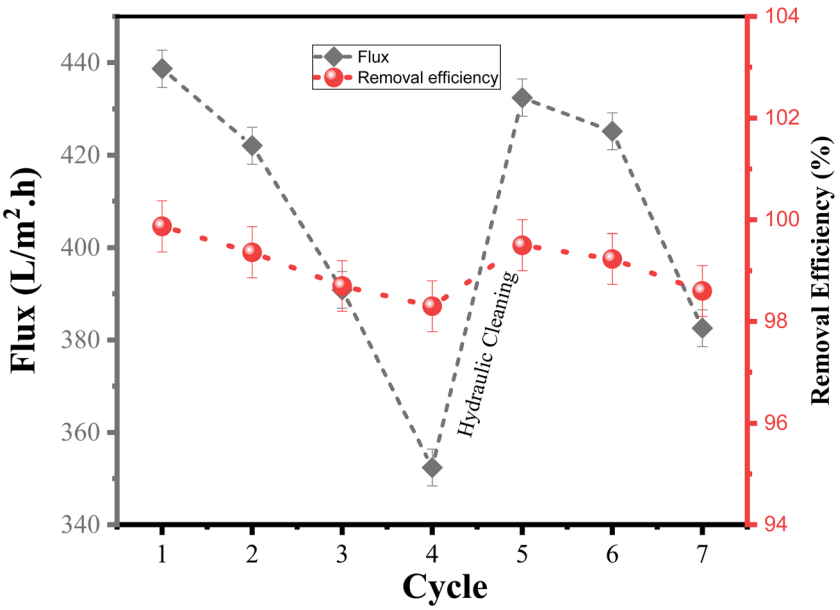

Fig. 16 Long-term stability studies of the optimal PVDF-TiO_2-nZVI-SiO_2 nanocomposite membrane using 5 ppm Pb^{2+} solution.

Fig. 15(a) shows the Cr(IV) rejection rate at various loadings on M5 membrane. The figures compared overall performance stability with efficiency of the optimum membrane. The results indicate that the Cr(VI) rejection rate declines as the initial concentration of Cr(VI) ions increases, with an average overall rejection rate of 92% across the Cr(VI) contaminant loadings, suggesting a balanced and effective removal efficiency throughout the filtration period. The sustained performance despite higher contaminants loading demonstrates the ability of the SiO_2 coating in preventing leaching and ensuring stabilization of nZVI-TiO_2 against aggregation. Despite the conventional principle that higher concentration of the contaminant results to a greater mass transfer resistance and potential blockage of catalytic active sites,[149] the rejection stability obtained in this study (>90% at higher Cr(IV) and Pb^{2+} concentrations) confirmed a continual availability of active sites from the nanocomposite membrane for the mineralization Pb^{2+} and chemical reduction of Cr(VI) to Cr^{3+}.

In Fig. 15(b) the rejection rate of Cr(VI) and Pb^{2+} at 20 ppm, 30 ppm, 40 ppm, and 50 ppm were compared with the filtration

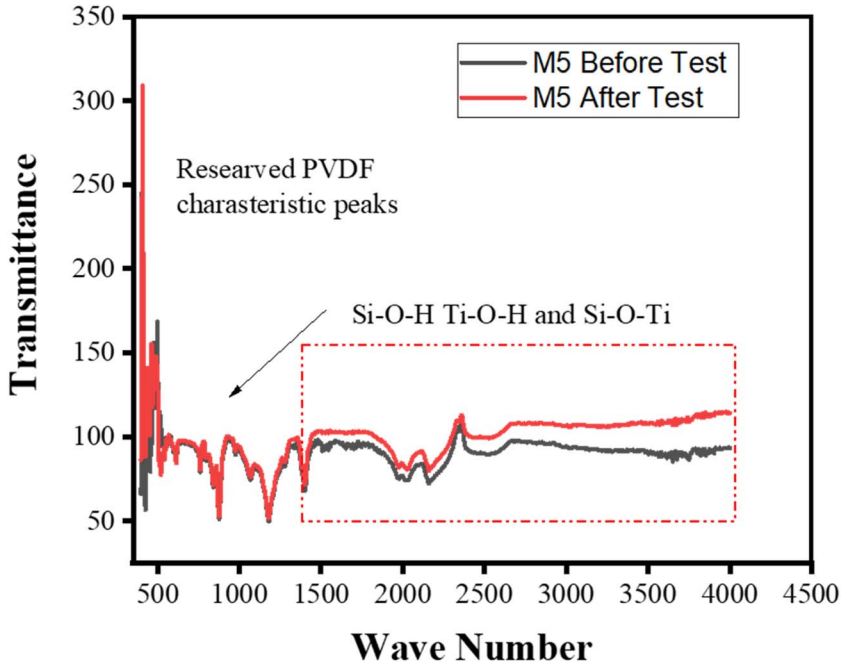

Fig. 17 FTIR spectra comparing the optimal PVDF-TiO_2-nZVI-SiO_2 nanocomposite membrane before and after Pb^{2+} treatment.

time to evaluate the influence of normalized filtration time, flux stability and membrane performance.

The long-term stability and reusability of the developed PVDF-TiO_2-nZVI-SiO_2 optimal nanocomposite membrane was investigated through 5 ppm Pb^{2+} solution over 7 cycles of filtration operation as shown in Fig. 16. A slow flux decrease was observed after 4.7 hours of filtration operation, attributable to the accumulation of surface foulants. However, the membrane flux was regenerated following hydraulic cleaning treatment. Furthermore, the separation efficiency remained above 98% confirming the stability and structural integrity of the PVDF-TiO_2-nZVI-SiO_2 nanocomposite membrane. FTIR analysis of the optimal membrane (refer to Fig. 17) was further conducted and compared with spectral peaks before reusability analysis. The results from this analysis corroborate a consistent hydraulic and anti-fouling performance of the optimum nanocomposite membrane associated with influence of enhanced hydrophilic properties,[43,52] observed in the water contact angle analysis discussed in the previous section. The hydrophilic properties and flux stability of the developed nanocomposite membrane is a crucial finding of this study that contribute to the operational challenges in practical membrane applications particularly where there is an intermittent flux decline or a trade-off between membrane hydraulic properties and membrane purification performance.

The FTIR spectra comparing the PVDF-TiO_2-nZVI-SiO_2 nanocomposite membrane M5 before and after Pb^{2+} treatment is shown in Fig. 17. The results revealed changes in peak intensities and provided molecular insight on the Pb^{2+} chemisorption removal process with the functional groups on the membrane surface. The change in peaks intensities and shift of the O–H stretching vibrations peaks observed around 3000 to 3500 cm^{-1} regions indicate active participation of these functional groups in binding Pb^{2+} ions. Furthermore, there is an observed changes in the shape and positions of Si–O, Fe–O peaks at 1000–1200 cm^{-1}, these spectral changes corroborate the formation of a chemical bond or chelation complex between the Pb^{2+} ions and the oxygen-containing functional groups of the PVDF-TiO_2-nZVI-SiO_2 nanocomposite which could be basis for the high R^2 value observed in the PSO studies (refer to S2).

4 Conclusion

In conclusion, this study provided a comprehensive investigation of the synthesis, characterization, and performance evaluation of a novel PVDF-TiO_2-nZVI-SiO_2 nanocomposite membrane for the removal of Cr(VI) and Pb^{2+} from aqueous solutions. The physicochemical properties of the synthesized TiO_2-nZVI-SiO_2 nanocomposite were investigated *via* various techniques with XPS and TGA analysis confirming the thermal stability and successful coating of the SiO_2 on the TiO_2-nZVI surface. The developed PVDF-TiO_2-nZVI-SiO_2 nanocomposite membrane showed stable hydraulic properties, enhanced hydrophilicity and long-term stability. The optimum nanocomposite loading (M5) was determined and the Pb^{2+} removal was found to be higher, 99.8% compared to Cr(VI) 94.3% which required the formation of Cr^{3+} prior to co-precipitation and membrane matrix retention. The removal efficiencies exceed 90% across all nanocomposite membranes and contaminants loadings.

Author contributions

All authors contributed to the study conception and design. Material preparation, experiments, analysis and writing the first draft were performed by Murtala Namakka. And all authors commented on previous versions of the manuscript. All authors read and approved of the final manuscript.

Conflicts of interest

The authors have no relevant financial or non-financial interests to disclose.

Data availability

Data described in this research are provided in the supplementary information (SI) file. Supplementary information is available. See DOI: https://doi.org/10.1039/d5ra08723f.

Acknowledgements

This work was funded by Universiti Malaysia Sarawak under the Vice Chancellor Higher Impact Research Scheme, Grant Number (UNI/FO2/VC-HIRG/85508/P10-03).

References

1 M. Herrera, X. Xie, A. Menapace, A. Zanfei and B. M. Brentan, Sustainable AI infrastructure: A scenario-based forecast of water footprint under uncertainty, *J. Clean. Prod.*, 2025, **526**(August), 146528, DOI: 10.1016/j.jclepro.2025.146528.

2 J. Cowls, A. Tsamados, M. Taddeo and L. Floridi, The AI gambit: leveraging artificial intelligence to combat climate change—opportunities, challenges, and recommendations, *AI Soc.*, 2023, **38**(1), 283–307, DOI: 10.1007/s00146-021-01294-x.

3 Y. Zhao, W. Yu, R. Li, Y. Xu, Y. Liu, T. Sun, *et al.*, Electric field endowing the conductive polyvinylidene fluoride (PVDF)-graphene oxide (GO)-nickel (Ni) membrane with high-efficient performance for dye wastewater treatment, *Appl. Surf. Sci.*, 2019, **483**(January), 1006–1016, DOI: 10.1016/j.apsusc.2019.04.054.

4 S. M. Botsa, Reduced graphene oxide – assisted TiO_2 – Fe_2O_3 ternary nanocomposite for efficient visible – light driven photocatalysis of nitrobenzene and dye pollutants, *Adv. Compos. Hybrid Mater.*, 2025, **8**, 384, DOI: 10.1007/s42114-025-01431-w.

5 G. Jingling, Y. S. Bin Xiang and J. Li, Janus smart materials with asymmetrical wettability for on-demand oil/water separation: a comprehensive review, *J. Mater. Chem. A*, 2023, **11**(46), 25093–25114. https://pubs.rsc.org/en/content/articlelanding/2023/ta/d3ta04160c.

6 H. An, T. Liu, X. Xiao, M. Liu, Y. Hu, P. Wei, *et al.*, Magnetic biochar-supported nanoscale zero-valent iron for remediation of arsenic and cadmium-contaminated soils: The role of free radicals, *Environ. Res.*, 2025, **276**, 121484, DOI: 10.1016/j.envres.2025.121484.

7 C. Zhang, D. Shi, C. Wang, G. Sun, H. Li, Y. Hu, *et al.*, Pristine/magnesium-loaded biochar and ZVI affect rice grain arsenic speciation and cadmium accumulation through different pathways in an alkaline paddy soil, *J. Environ. Sci.*, 2024, **147**, 630–641.

8 H. Alijani and Z. Shariatinia, Effective aqueous arsenic removal using zero valent iron doped MWCNT synthesized by in situ CVD method using natural α-Fe2O3as a precursor, *Chemosphere*, 2017, **171**, 502–511, DOI: 10.1016/j.chemosphere.2016.12.106.

9 A. Khan, S. Ahmad, M. Nafees, Z. Mahmood, S. Ali, W. Du, *et al.*, Chemosphere Alleviated cadmium toxicity in wheat (Triticum aestivum L.) by the coactive role of zinc oxide nanoparticles and plant growth promoting rhizobacteria on TaEIL1 gene expression , biochemical and physiological changes, *Chemosphere*, 2024, **364**, 143113, DOI: 10.1016/j.chemosphere.2024.143113.

10 V. Khum-in, J. Suk-in, P. In-ai, K. Piaowan, Y. Praimeesub, K. Rintachai, *et al.*, Combining magnet-assisted soil washing and soil amendment with zero-valent iron to restore safe rice cultivation in real cadmium-contaminated paddy fields, *Chemosphere*, 2023, **340**, 139816, DOI: 10.1016/j.chemosphere.2023.139816.

11 S. Xie, Water contamination due to hexavalent chromium and its health impacts: exploring green technology for Cr (VI) remediation, *Green Chem. Lett. Rev.*, 2024, **17**(1), 1–19, DOI: 10.1080/17518253.2024.2356614.

12 Z. Ren, H. Tang, H. Li and Q. Jing, Journal of Water Process Engineering Column experimental study on the removal of hexavalent chromium from water by modified cellulose filter paper loaded with nano zero-valent iron, *J. Water Proc. Eng.*, 2024, **59**, 104920, DOI: 10.1016/j.jwpe.2024.104920.

13 L. Zhang, Y. Zhu, H. Gu, S. S. Lam, X. Chen, C. Sonne, *et al.*, A review of phytoremediation of environmental lead (pb) contamination, *Chemosphere*, 2024, **362**, 142691, DOI: 10.1016/j.chemosphere.2024.142691.

14 W. Zhan, Y. Yuan, X. Zhang, Y. Liang, S. Song, M. de Jesús Martínez-López, *et al.*, Efficient and selective Lead(II) removal within a wide concentration range through chemisorption and electrosorption coupling process via defective MoS2 electrode, *Sep. Purif. Technol.*, 2024, **329**, 125183, DOI: 10.1016/j.seppur.2023.125183.

15 M. A. Irshad, S. Sattar, R. Nawaz, S. A. Al-Hussain, M. Rizwan, A. Bukhari, *et al.*, Enhancing chromium removal and recovery from industrial wastewater using sustainable and efficient nanomaterial: A review, *Ecotoxicol. Environ. Saf.*, 2023, **263**, 115231, DOI: 10.1016/j.ecoenv.2023.115231.

16 I. R. Chowdhury, S. Chowdhury, M. A. J. Mazumder and A. Al-Ahmed, Removal of lead ions (Pb2+) from water and wastewater: a review on the low-cost adsorbents, *Appl. Water Sci.*, 2022, **12**, 1–33, DOI: 10.1007/s13201-022-01703-6.

17 V. Kumar, S. K. Dwivedi and S. Oh, A critical review on lead removal from industrial wastewater: Recent advances and future outlook, *J. Water Proc. Eng.*, 2022, **45**(2021), 102518, DOI: 10.1016/j.jwpe.2021.102518.

18 Q. Chen, Z. Luo, C. Hills, G. Xue and M. Tyrer, Precipitation of heavy metals from wastewater using simulated flue gas: Sequent additions of fly ash, lime and carbon dioxide, *Water Res.*, 2009, **43**(10), 2605–2614, DOI: 10.1016/j.watres.2009.03.007.

19 M. C. Benalia, L. Youcef, M. G. Bouaziz, S. Achour and H. Menasra, Removal of Heavy Metals from Industrial Wastewater by Chemical Precipitation: Mechanisms and Sludge Characterization, *Arabian J. Sci. Eng.*, 2022, **47**(5), 5587–5599, DOI: 10.1007/s13369-021-05525-7.

20 E. Sgreccia, C. Rogalska, F. S. Gallardo Gonzalez, P. Prosposito, L. Burratti, P. Knauth, *et al.*, Heavy metal decontamination by ion exchange polymers for water purification: counterintuitive cation removal by an anion exchange polymer, *J. Mater. Sci.*, 2024, **59**(7), 2776–2787, DOI: 10.1007/s10853-024-09356-3.

21 A. Q. Jasim and S. K. Ajjam, Removal of heavy metal ions from wastewater using ion exchange resin in a batch process with kinetic isotherm, *S. Afr. J. Chem. Eng.*, 2024, **49**, 43–54, DOI: 10.1016/j.sajce.2024.04.002.

22 Z. Wang, Z. Tan, H. Li, S. Yuan, Y. Zhang and Y. Dong, Direct current electrochemical method for removal and recovery of heavy metals from water using straw biochar electrode, *J. Clean. Prod.*, 2022, **339**, 130746, DOI: 10.1016/j.jclepro.2022.130746.

23 E. C. Okpara, O. E. Fayemi, O. B. Wojuola, D. C. Onwudiwe and E. E. Ebenso, Electrochemical detection of selected heavy metals in water: a case study of African experiences, *RSC Adv.*, 2022, **12**(40), 26319–26361.

24 E. H. Khader, S. A. Muslim, N. M. C. Saady, N. S. Ali, I. K. Salih, T. J. Mohammed, *et al.*, Recent advances in photocatalytic advanced oxidation processes for organic compound degradation: A review, *Desalination Water Treat.*, 2024, **318**, 100384, DOI: 10.1016/j.dwt.2024.100384.

25 B. Yan, Y. Dai, L. Xin, M. Li, H. Zhang, H. Long, *et al.*, Research progress in the degradation of printing and dyeing wastewater using chitosan based composite photocatalytic materials, *Int. J. Biol. Macromol.*, 2024, **263**, 130082, DOI: 10.1016/j.ijbiomac.2024.130082.

26 T. Munawar, F. Mukhtar, K. M. Batoo, A. Mazhar, M. S. Nadeem, S. Hussain, *et al.*, Sunlight-activated Mo-doped La2CuO4/rGO perovskite oxide nanocomposite for photocatalytic treatment of diverse dyes pollutant, *Mater. Sci. Eng. B*, 2024, **304**, 117355, DOI: 10.1016/j.mseb.2024.117355.

27 D. Fatta-Kassinos, M. I. Vasquez and K. Kümmerer, Transformation products of pharmaceuticals in surface waters and wastewater formed during photolysis and advanced oxidation processes - Degradation, elucidation of byproducts and assessment of their biological potency,

Chemosphere, 2011, **85**(5), 693–709, DOI: 10.1016/j.chemosphere.2011.06.082.

28 L. Rizzo, Bioassays as a tool for evaluating advanced oxidation processes in water and wastewater treatment, *Water Res.*, 2011, **45**(15), 4311–4340, DOI: 10.1016/j.watres.2011.05.035.

29 C. R. Holkar, A. J. Jadhav, D. V. Pinjari, N. M. Mahamuni and A. B. Pandit, A critical review on textile wastewater treatments: Possible approaches, *J. Environ. Manage.*, 2016, **182**, 351–366, DOI: 10.1016/j.jenvman.2016.07.090.

30 W. S. Chai, J. Y. Cheun, P. S. Kumar, M. Mubashir, Z. Majeed, F. Banat, *et al.*, A review on conventional and novel materials towards heavy metal adsorption in wastewater treatment application, *J. Clean. Prod.*, 2021, **296**, 126589, DOI: 10.1016/j.jclepro.2021.126589.

31 B. He, W. Zhang, Y. Diao, S. Sun, Y. Zhang, W. Zhao, *et al.*, Mechanistic study of the adsorption capabilities of heavy metals on the surface of ferrihydrite: batch sorption, modeling, and density functional theory, *RSC Adv.*, 2025, **15**(2), 1072–1080.

32 L. Mohapatra, Y. F. Tsang, X. Dou and K. Baek, MnFe-layered double hydroxides grown on spherical SiO2 to construct core-shell heterostructures for enhanced simultaneous photocatalytic redox Reactions of Cr(VI) and As(III), *J. Water Proc. Eng.*, 2022, **50**, 103236, DOI: 10.1016/j.jwpe.2022.103236.

33 Q. Jing, W. You, S. Qiao, Y. Ma and Z. Ren, Comprehensive understanding of adsorption and reduction on 2,4-DCP and Cr(VI) removal process by NZVI-rGO: Performance and mechanism, *J. Water Proc. Eng.*, 2023, **51**, 103413, DOI: 10.1016/j.jwpe.2022.103413.

34 R. Fu, Y. Yang, Z. Xu, X. Zhang, X. Guo and D. Bi, The removal of chromium (VI) and lead (II) from groundwater using sepiolite-supported nanoscale zero-valent iron (S-NZVI), *Chemosphere*, 2015, **138**, 726–734, DOI: 10.1016/j.chemosphere.2015.07.051.

35 M. Kazemi, M. Peyravi and M. Jahanshahi, Multilayer UF membrane assisted by photocatalytic NZVI@TiO2 nanoparticle for removal and reduction of hexavalent chromium, *J. Water Proc. Eng.*, 2020, **37**, 101183, DOI: 10.1016/j.jwpe.2020.101183.

36 A. M. Zafar, A. Naeem, M. A. Minhas, M. J. Hasan, S. Rafique and A. Ikhlaq, Removal of reactive dyes from textile industrial effluent using electrocoagulation in different parametric conditions of aluminum electrodes, *Total Environ. Adv.*, 2024, **9**, 200087, DOI: 10.1016/j.teadva.2023.200087.

37 Z. Hejri, M. Hejri, M. Omidvar and S. Morshedi, Synthesis of TiO2/nZVI nanocomposite for nitrate removal from aqueous solution, *Int. J. Ind. Chem.*, 2019, **10**(3), 225–236, DOI: 10.1007/s40090-019-0186-3.

38 M. Zhao, Z. Niu, Y. Xu, F. Fan, W. Wu and D. Pan, One-step electrospinning preparation of magnetic NZVI@TiO2 nanofibers for enhanced immobilization of U(VI) from aqueous solution, *J. Radioanal. Nucl. Chem.*, 2023, **332**(4), 1083–1091, DOI: 10.1007/s10967-022-08696-1.

39 M. Namakka and R. Rahman, RSC Advances Insights into micro-and nano-zero valent iron materials : synthesis methods and multifaceted applications, *RSC Adv.*, 2024, **14**, 30411–30439, DOI: 10.1039/D4RA03507K.

40 M. Namakka, M. R. Rahman, K. A. Mohamad Bin Said, K. K. Kuok, F. A. Md Yusof, M. S. M. Al-Saleem, *et al.*, Unveiling the synergistic effect of an nZVI–SiO 2 –TiO 2 nanocomposite for the remediation of dye contaminated wastewater, *Mater. Adv.*, 2024, 9292–9313, DOI: 10.1039/d4ma00853g.

41 M. Namakka, M. R. Rahman, K. A. Mohamad Bin Said, K. K. Kuok, F. A. Md Yusof, M. S. M. Al-Saleem, *et al.*, Unveiling the synergistic effect of an nZVI–SiO 2 –TiO 2 nanocomposite for the remediation of dye contaminated wastewater, *Mater. Adv.*, 2024, 9292–9313, DOI: 10.1039/d4ma00853g.

42 S. S. Koçak, O. S. Özdemir, M. Asiltürk and İ. Atmaca, Thermal and Optical Characteristics of TiO2@SiO2, Fe3O4@SiO2, and ZnO@SiO2 Core–Shell Nanoparticles and Their Water-Based Nanofluids, *Int. J. Thermophys.*, 2025, **46**, 3–38, DOI: 10.1007/s10765-025-03558-w.

43 H. Nawaz, M. Umar, A. Ullah, H. Razzaq, K. M. Zia and X. Liu, Polyvinylidene fluoride nanocomposite super hydrophilic membrane integrated with Polyaniline-Graphene oxide nano fillers for treatment of textile effluents, *J. Hazard. Mater.*, 2021, **403**, 123587, DOI: 10.1016/j.jhazmat.2020.123587.

44 M. R. Rahman, A. James, M. Said, M. Namakka, M. U. Khandaker, W. H. Jiunn, J. Y. Al-Humaidi, R. H. Althomali and M. M. Rahman, A TiO2 grafted bamboo derivative nanocellulose polyvinylidene fluoride (PVDF) nanocomposite membrane for wastewater treatment by a photocatalytic process, *Mater. Adv.*, 2024, 7617–7636, DOI: 10.1039/d4ma00716f.

45 D. Sharma, S. Kanchi and K. Bisetty, Biogenic synthesis of nanoparticles: A review., *Arab. J. Chem.*, 2019, **12**, 3576–3600.

46 S. Aziz and A. Abdel-Karim, Dual-functional ultrafiltration biocatalytic membrane containing laccase/nanoparticle for removal of pollutants: A review, *Environ. Nanotechnol. Monit. Manag.*, 2023, **20**, 100852, DOI: 10.1016/j.enmm.2023.100852.

47 G. H. Major, V. Fernandez, N. Fairley, E. F. Smith and M. R. Linford, Guide to XPS data analysis: Applying appropriate constraints to synthetic peaks in XPS peak fitting, *J. Vac. Sci. Technol. A*, 2022, **40**(6), 063201, DOI: 10.1116/6.0001975.

48 A. C. Baily, T. Nunney, Thermo Fisher Scientific, East Grinstead, West Sussex, UK, *XPS Analysis of a Hard Disk Platter by Rapid Depth Profiling*, 2019.

49 A. James, M. Rezaur Rahman, K. Anwar Mohamed Said, M. Namakka, K. Kuok Kuok, M. Uddin Khandaker, *et al.*, Lithium Chloride-Mediated enhancement of dye removal capacity in Borneo bamboo derived nanocellulose-based nanocomposite membranes (NCMs), *J. Mol. Liq.*, 2024, **413**, 125973, DOI: 10.1016/j.molliq.2024.125973.

50 ASTM F3419-22. ASTM International, *Standard Test Method for Mineral Characterization of Equine Surface Materials by X-Ray Diffraction (XRD) Techniques*, West Conshohocken, PA, USA, 2022.
51 M. R. Rahman, A. Z. Sueraya, K. A. B. M. Said, M. Namakka, A. James, I. M. M. Rahman, *et al.*, Impact of Graphene/Nanocellulose on Nanocomposite Membrane for Methylene Blue Dye Removal and Antifouling Performance, *J. Appl. Polym. Sci.*, 2025, 1–21.
52 G. Hurwitz, G. R. Guillen and E. M. V. Hoek, Probing polyamide membrane surface charge, zeta potential, wettability, and hydrophilicity with contact angle measurements, *J. Membr. Sci.*, 2010, **349**(1–2), 349–357.
53 T. Iqbal, R. Sahrash, A. Siddiqa, S. Afsheen, M. B. Tahir, M. I. Khan, *et al.*, Preparation and characterization of polyvinylidene fluoride/1-butyl-3-methylimidazolium bromide-based ionogel membranes for desalination applications, *Int. J. Environ. Sci. Technol.*, 2019, **16**(11), 7081–7092, DOI: 10.1007/s13762-019-02207-8.
54 C. S. Ong, W. J. Lau, P. S. Goh, B. C. Ng, T. Matsuura and A. F. Ismail, Effect of PVP Molecular Weights on the Properties of PVDF-TiO2 Composite Membrane for Oily Wastewater Treatment Process, *Separ. Sci. Technol.*, 2014, **49**(15), 2303–2314.
55 P. L. N. Khui, M. R. Rahman, K. A. bin M. Said, M. Namakka, M. Shahabuddin, M. S. M. Al-Saleem, *et al.*, Enhanced flux and surface modification of PVDF hollow fiber membranes using bamboo cellulose/PVA composite coatings, *Polym. Bull.*, 2025, (0123456789), 12909–12927, DOI: 10.1007/s00289-025-06023-8.
56 R. Razavi, A. Shakeri and H. Salehi, A novel thin film nanocomposite forward osmosis membrane modified with zwitterionic GO-g-PSBMA with high fouling resistance and heavy metal ions rejection, *J. Environ. Chem. Eng.*, 2025, **13**(1), 115308, DOI: 10.1016/j.jece.2025.115308.
57 M. R. Rahman, A. Z. Sueraya, K. A. B. M. Said, M. Namakka, A. James, I. M. M. Rahman, *et al.*, Impact of Graphene/Nanocellulose on Nanocomposite Membrane for Methylene Blue Dye Removal and Antifouling Performance, *J. Appl. Polym. Sci.*, 2025, 1–21.
58 M. Namakka, M. R. Rahman, K. A. Bin Mohamad Said and A. Muhammad, Insights into micro-and nano-zero valent iron materials: synthesis methods and multifaceted applications, *RSC Adv.*, 2024, **14**(41), 30411–30439.
59 R. Zhang, R. Napolano, B. Xi, A. M. Salazar, Q. Shi, Y. Zhao, *et al.*, Mechanistic insights into Cr(VI) removal by a combination of zero-valent iron and pyrite, *Chemosphere*, 2023, **330**, 138693, DOI: 10.1016/j.chemosphere.2023.138693.
60 Q. B. Nguyen, C. Kim and I. Hwang, Roles of silica coating on nanosized zero-valent iron in sequential reduction–oxidation process in a system containing persulfate, *J. Hazard. Mater.*, 2024, **480**, 135946, DOI: 10.1016/j.jhazmat.2024.135946.
61 P. Y. Jia, X. M. Liu, G. Z. Li, M. Yu, J. Fang and J. Lin, Sol-gel synthesis and characterization of SiO2@CaWO 4,SiO2@CaWO4:Eu3+/Tb3+ core-shell structured spherical particles, *Nanotechnology*, 2006, **17**(3), 734–742.
62 S. Saravanan, R. S. Dubey, S. Saravanan and R. S. Dubey, Synthesis of SiO2 Nanoparticles by Sol-Gel Method and Their Optical and Structural Properties Thin films for Opto-Electronic Applications View project Nanomaterials View project Synthesis of SiO2 Nanoparticles by Sol-Gel Method and Their Optical and Structural Properties, *Rom. J. Inf. Sci. Technol.*, 2020, **23**, 1. https://www.researchgate.net/publication/338828540.
63 C. Ratanaphain, D. Viboonratanasri, P. Prompinit, S. Krajangpan, E. Khan and P. Punyapalakul, Mechanistic study of iodoacetamide degradation by functionalized SiO2-coated nZVI: The role of surface functional groups on adsorption, dehalogenation and hydrolysis, *J. Water Proc. Eng.*, 2024, **63**, 105485, DOI: 10.1016/j.jwpe.2024.105485.
64 A. Rosales and K. Esquivel, SiO2@TiO2 composite synthesis and its hydrophobic applications: A review, *Catalysts*, 2020, **10**(2), 1–17, DOI: 10.3390/catal10020171.
65 Z. Liu, G. Chen, F. Hu and X. Li, Synthesis of mesoporous magnetic MnFe2O4@CS-SiO2 microsphere and its adsorption performance of Zn2+ and MB studies, *J. Environ. Manage.*, 2020, **263**, 110377, DOI: 10.1016/j.jenvman.2020.110377.
66 Q. Li, H. Wang, Z. Chen, X. He, Y. Liu, M. Qiu, *et al.*, Adsorption-reduction strategy of U(VI) on NZVI-supported zeolite composites via batch, visual and XPS techniques, *J. Mol. Liq.*, 2021, **339**, 116719, DOI: 10.1016/j.molliq.2021.116719.
67 M. Zhao, Z. Niu, Y. Xu, F. Fan, W. Wu and D. Pan, One-step electrospinning preparation of magnetic NZVI@TiO2 nanofibers for enhanced immobilization of U(VI) from aqueous solution, *J. Radioanal. Nucl. Chem.*, 2023, **332**(4), 1083–1091.
68 H. Hu, D. Zhao, C. Wu and R. Xie, Sulfidized Nanoscale Zerovalent Iron Supported by Oyster Powder for Efficient Removal of Cr (VI): Characterization, Performance, and Mechanisms, *Materials*, 2022, **15**(11), 1–16, DOI: 10.3390/ma15113898.
69 S. Xie, J. Su, J. Zhao, H. Yang and H. Qian, An amorphous zero-valent iron decorated by Fe3O4 significantly improves the Fenton-like reaction, *J. Alloys Compd.*, 2022, **929**, 167306, DOI: 10.1016/j.jallcom.2022.167306.
70 M. Namakka, M. R. Rahman, K. A. M. B. Said, M. Abdul Mannan and A. M. Patwary, A review of nanoparticle synthesis methods, classifications, applications, and characterization, *Environ. Nanotechnol. Monit. Manag.*, 2023, **20**, 100900, DOI: 10.1016/j.enmm.2023.100900.
71 L. Liu, J. Zhao, X. Liu, S. Bai, H. Lin and D. Wang, Reduction and removal of As(V) in aqueous solution by biochar derived from nano zero-valent-iron (nZVI) and sewage sludge, *Chemosphere*, 2021, **277**, 130273, DOI: 10.1016/j.chemosphere.2021.130273.
72 J. Hou, Y. Li, H. Ci, L. Miao, G. You, J. Wu, *et al.*, Influence of aggregation and sedimentation behavior of bare and modified zero-valent-iron nanoparticles on the Cr(VI)

removal under various groundwater chemistry conditions, *Chemosphere*, 2022, **296**, 133905, DOI: 10.1016/j.chemosphere.2022.133905.

73 Y. P. Sun, X. Q. Li, J. Cao, W. X. Zhang and H. P. Wang, Characterization of zero-valent iron nanoparticles, *Adv. Colloid Interface Sci.*, 2006, **120**(1–3), 47–56.

74 M. M. El-shafei, A. Hamdy and M. M. Hefny, Zero-valent iron nanostructures: synthesis, characterization and application, *J. Environ. Biotechnol. Res.*, 2018, **7**, 1–10.

75 W. Li, R. Liang, A. Hu, Z. Huang and Y. N. Zhou, Generation of oxygen vacancies in visible light activated one-dimensional iodine TiO2 photocatalysts, *RSC Adv.*, 2014, **4**(70), 36959–36966, DOI: 10.1039/C4RA04768K.

76 N. Prabhakar, A. M. Isloor, M. Padaki and A. Fauzi Ismail, Fabrication of TiO2@ZIF-67 metal organic framework composite incorporated PVDF membranes for the removal of hazardous reactive black 5 and Congo red dyes from contaminated water, *Chem. Eng. J.*, 2024, **498**, 155270, DOI: 10.1016/j.cej.2024.155270.

77 S. Kalidhasan and H. Y. Lee, Preparation of TiO2-deposited silica-based catalysts for photocatalytic decomposition of chloro-pesticide to environmentally less toxic species, *Chemosphere*, 2022, **290**, 133300, DOI: 10.1016/j.chemosphere.2021.133300.

78 W. Biao, N. Awanis Hashim, M. F. B. Rabuni, O. Lide and A. Ullah, An innovative strategy for polyester microplastic fiber elimination from laundry wastewater via coupled separation and degradation using TiO2-based photocatalytic membrane reactor, *Sep. Purif. Technol.*, 2025, **356**, 129929, DOI: 10.1016/j.seppur.2024.129929.

79 C. G. Soria-Hernández, L. M. Palacios-Pineda, A. Elías-Zúñiga, I. A. Perales-Martínez and O. Martínez-Romero, Investigation of the effect of carbonyl iron micro-Particles on the mechanical and rheological properties of isotropic and anisotropic MREs: Constitutive magneto-mechanical material model, *Polymers*, 2019, **11**(10), 2–22, DOI: 10.3390/polym11101705.

80 Y. Chen, X. F. Zhang, A. J. Wang, Q. L. Zhang, H. Huang and J. J. Feng, Ultrafine Fe3C nanoparticles embedded in N-doped graphitic carbon sheets for simultaneous determination of ascorbic acid, dopamine, uric acid and xanthine, *Microchim. Acta*, 2019, **186**(9), 660, DOI: 10.1007/s00604-019-3769-y.

81 S. Mallakpour and M. Naghdi, Application of SiO2 nanoparticles with double layer coverage consist of citric acid and l(+)-ascorbic acid for the production of poly(vinyl chloride)/SiO2 nanocomposite films with enhanced optical and thermal properties, *Polym. Bull.*, 2016, **73**(6), 1701–1717.

82 S. H. Ammar, A. Ibrahim Elaibi and Sh. Mohammed I, Core/shell Fe3O4@Al2O3-PMo magnetic nanocatalyst for photocatalytic degradation of organic pollutants in an internal loop airlift reactor, *J. Water Proc. Eng.*, 2020, **37**, 101240, DOI: 10.1016/j.jwpe.2020.101240.

83 A. S. Astuti, M. Muldarisnur and U. S. R. A. Zulhadjri, Enhancement in photoluminescence performance of carbon-based Fe3O4@ZnO–C nanocomposites, *Vacuum*, 2023, **211**, 111935, DOI: 10.1016/j.vacuum.2023.111935.

84 M. Yaghoobi, F. Asjadi and M. Sanikhani, A facile one-step green hydrothermal synthesis of paramagnetic Fe3O4 nanoparticles with highly efficient dye removal, *J. Taiwan Inst. Chem. Eng.*, 2023, 144.

85 N. Lertthanaphol, P. Sereerattanakorn, S. Tulaphol, T. Maihom, T. K. Phung, G. Garbarino, *et al.*, Selective conversion of aqueous sorbitol to sorbitan by amorphous Silica-Alumina catalysts, *Chem. Eng. J.*, 2025, **511**, 161918, DOI: 10.1016/j.cej.2025.161918.

86 A. Perzon and P. Ulvskov, Journal Pre of, *Solid State Sci.*, 2019, 108117, DOI: 10.1016/j.solidstatesciences.2025.108117.

87 S. Madan, R. Shaw, S. Tiwari and S. K. Tiwari, Enhancing corrosion stability and shelf life of nanoscale zero-valent iron via encapsulation in porous Ze-TiO2 matrix: An interface for simultaneous oxidation and adsorption of As(III), *Colloids Surf., A*, 2020, **607**, 125381, DOI: 10.1016/j.colsurfa.2020.125381.

88 Q. Li, H. Wang, Z. Chen, X. He, Y. Liu, M. Qiu, *et al.*, Adsorption-reduction strategy of U(VI) on NZVI-supported zeolite composites via batch, visual and XPS techniques, *J. Mol. Liq.*, 2021, **339**, 116719, DOI: 10.1016/j.molliq.2021.116719.

89 X. Li, M. Gao, Y. Huo, H. Liu, J. Li, T. Huang, *et al.*, Impacts of shell structure on nitrate-reduction activity and air stability of nanoscale zero-valent iron, *Environ. Sci. Pollut. Res.*, 2022, **29**(53), 80683–80692, DOI: 10.1007/s11356-022-21460-y.

90 L. Wang, C. Song, X. Jiang, T. Li and H. Wang, Mechanochemical synthesis of redox-active Fe-based nanocomposites for efficient Cr(VI) remediation in water and soil, *Sep. Purif. Technol.*, 2025, **377**, 134212, DOI: 10.1016/j.seppur.2025.134212.

91 L. Guo, Synthesis of Amorphous-Coated and Amorphous-Doped Nanomaterials, in *Amorphous Nanomaterials*, ed. L. Guo, 2021, DOI: 10.1002/9783527826360.ch8.

92 B. Alessi, M. Macias-Montero, C. Maddi, P. Maguire, V. Svrcek and D. Mariotti, Bridging energy bands to the crystalline and amorphous states of Si QDs, *Faraday Discuss.*, 2020, **222**, 390–404.

93 M. Kitabata, T. Taddese and S. Okazaki, Molecular Dynamics Study on Wettability of Poly(vinylidene fluoride) Crystalline and Amorphous Surfaces, *Langmuir*, 2018, **34**(40), 12214–12223.

94 P. J. Tapia, J. Gallego and J. F. Espinal, Calcination Temperature Effect in Catalyst Reactivity for the CO SELOX Reaction Using Perovskite-like LaBO3 (B: Mn, Fe, Co, Ni) Oxides, *Catal. Lett.*, 2021, **151**(12), 3690–3703, DOI: 10.1007/s10562-021-03601-z.

95 S. Jain, J. Shah, N. S. Negi, C. Sharma and R. K. Kotnala, Significance of interface barrier at electrode of hematite hydroelectric cell for generating ecopower by water splitting, *Int. J. Energy Res.*, 2019, **43**(9), 4743–4755.

96 H. Wu, L. Zheng, J. Zhan, N. Du, W. Liu, J. Ma, *et al.*, Recycling silicon-based industrial waste as sustainable

sources of Si/SiO2 composites for high-performance Li-ion battery anodes, *J. Power Sources*, 2020, **449**, 227513, DOI: 10.1016/j.jpowsour.2019.227513.

97 G. Greczynski and L. Hultman, C 1s Peak of Adventitious Carbon Aligns to the Vacuum Level: Dire Consequences for Material's Bonding Assignment by Photoelectron Spectroscopy, *ChemPhysChem*, 2017, **18**(12), 1507–1512.

98 X-ray TTSK alpha. Investigating the oxidation of a cobalt-based catalyst using X-ray photoelectron spectroscopy.

99 A. Bushell, P. Mack, E. Grinstead and W. Sussex, *Identifying Structures on a Plasma-Modified Polymer Surface Authors*, Thermo Fisher Scientific Inc., 2019, AN52333_E:3.

100 T. T. Scientific, *Depth Profiling of an Organic FET with XPS and Argon Cluster Ions, Application Note*, 2019.

101 Y. C. G. Kwan, G. M. Ng and C. H. A. Huan, Identification of functional groups and determination of carboxyl formation temperature in graphene oxide using the XPS O 1s spectrum, *Thin Solid Films*, 2015, **590**, 40–48, DOI: 10.1016/j.tsf.2015.07.051.

102 G. Greczynski, D. Primetzhofer and L. Hultman, Reference binding energies of transition metal carbides by core-level x-ray photoelectron spectroscopy free from Ar + etching artefacts, *Appl. Surf. Sci.*, 2018, **436**, 102–110, DOI: 10.1016/j.apsusc.2017.11.264.

103 O. Wilhelmsson, S. Bijelovic, M. Lindquist, B. André, U. Wiklund, P. Svedlindh, *et al.*, Deposition and characterization of magnetic Ti-Fe-C nanocomposite thin films, *Thin Solid Films*, 2010, **518**(10), 2607–2616, DOI: 10.1016/j.tsf.2009.07.195.

104 X. Yu, L. Jiajun, Y. Xianglin, Z. Feng, L. Yongjun and L. Junbo, Preparation of graphdiyne-doped TiO2/SiO2 composite for enhanced photocatalytic activity, *J. Nanopart. Res.*, 2020, **22**(12), 365, DOI: 10.1007/s11051-020-05097-x.

105 S. Reghunath, D. Pinheiro and S. D. KR, A review of hierarchical nanostructures of TiO2: Advances and applications, *Appl. Surf. Sci. Adv.*, 2021, **3**, 100063, DOI: 10.1016/j.apsadv.2021.100063.

106 P. Yu, H. Yu, Q. Sun and B. Ma, Filter paper supported nZVI for continuous treatment of simulated dyeing wastewater, *Sci. Rep.*, 2019, **9**(1), 1–8.

107 S. S. Koçak, O. S. Özdemir, M. Asiltürk and İ. Atmaca, Thermal and Optical Characteristics of TiO2@SiO2, Fe3O4@SiO2, and ZnO@SiO2 Core–Shell Nanoparticles and Their Water-Based Nanofluids, *Int. J. Thermophys.*, 2025, **46**, 1–31, DOI: 10.1007/s10765-025-03558-w.

108 A. Anand, D. Meena, K. K. Dey and M. C. Bhatnagar, Enhanced piezoelectricity properties of reduced graphene oxide (RGO) loaded polyvinylidene fluoride (PVDF) nanocomposite films for nanogenerator application, *J. Polym. Res.*, 2020, **27**(12), 1–11. https://link.springer.com/article/10.1007/s10965-020-02323-x.

109 H. Zhang, Y. Zhu and L. Li, Fabrication of PVDF/graphene composites with enhanced β phase via conventional melt processing assisted by solid state shear milling technology, *RSC Adv.*, 2020, **10**(6), 3391–3401. https://pubs.rsc.org/en/content/articlehtml/2020/ra/c9ra09459h.

110 A. Zaienah and S. Rezaur, Impact of titanium dioxide/graphene in polyvinylidene fluoride nanocomposite membrane to intensify methylene blue dye removal, *Antifouling Performance , and Reusability*, 2024, pp. 1–14.

111 N. Ismail, M. Essalhi, M. Rahmati, Z. Cui, M. Khayet and N. Tavajohi, Experimental and theoretical studies on the formation of pure β-phase polymorphs during fabrication of polyvinylidene fluoride membranes by cyclic carbonate solvents, *Green Chem.*, 2021, **23**(5), 2130–2147.

112 S. Acarer-Arat, M. Tüfekci, İ. Pir and N. Tüfekci, Nanocellulose in polyvinylidene fluoride (PVDF) membranes: assessing reinforcement impact and modelling techniques, *J. Environ. Chem. Eng.*, 2024, **12**(6), 114749.

113 W. Zhang, G. Wu, H. Zeng, Z. Li, W. Wu, H. Jiang, *et al.*, The preparation, structural design and application of electroactive poly (vinylidene fluoride) - based materials for wearable sensors and human energy harvesters, *Polymers*, 2023, **15**(13), 2766.

114 A. James, M. R. Rahman, S. K. A. B. Mohamad, M. Namakka, M. Shahabuddin, M. S. M. Al-Saleem, *et al.*, Multifunctional PVDF membranes incorporating graphene, TiO2, and nanocellulose: synergistic effects on filtration and antifouling performance, *RSC Adv.*, 2025, **15**(38), 31471–31497.

115 A. James, M. Rezaur Rahman, K. Anwar Mohamed Said, M. Namakka, K. Kuok Kuok, M. Uddin Khandaker, *et al.*, Lithium Chloride-Mediated enhancement of dye removal capacity in Borneo bamboo derived nanocellulose-based nanocomposite membranes (NCMs), *J. Mol. Liq.*, 2024, **413**, 125973, DOI: 10.1016/j.molliq.2024.125973.

116 A. Ramazani, Z. Shaghaghi, H. Aghahosseini, P. A. Asiabi and S. W. Joo, Silica nanoparticles as a highly efficient catalyst for the onepot synthesis of sterically congested 2-(dibenzylamino)-2-Aryl acetamide derivatives from by phthaldehyde isomers, isocyanides and dibenzylamine, *Bull. Chem. Soc. Ethiop.*, 2016, **30**(3), 413–420.

117 M. Pyo, S. Jeong, J. H. Kim, M. J. Jeon and E. J. Lee, Hydrophobicity and membrane distillation performance of glass fiber membranes modified by dip coating of pure PDMS, *J. Environ. Chem. Eng.*, 2024, **12**(3), 112534, DOI: 10.1016/j.jece.2024.112534.

118 K. M. Jeong, Y. Li, D. G. Yoo, N. K. Lee, H. G. Lee, S. Ando, *et al.*, Effects of crosslinking agents on the physical properties of polyimide/amino-functionalized graphene oxide hybrid films, *Polym. Int.*, 2018, **67**(5), 588–597.

119 J. Sun, H. Bi, S. Su, H. Jia, X. Xie and L. Sun, One-step preparation of GO/SiO2 membrane for highly efficient separation of oil-in-water emulsion, *J. Membr. Sci.*, 2018, **553**, 131–138.

120 H. A. Budiarti, R. N. Puspitasari, A. M. Hatta and R. D. D. Sekartedjo, Synthesis and Characterization of TiO2@SiO2 and SiO2@TiO2 Core-Shell Structure Using Lapindo Mud Extract via Sol-Gel Method, *Procedia Eng.*, 2017, **170**, 65–71.

121 R. Liu, H. Jiang, P. Li, J. Yin, Z. Xu, X. Chen, *et al.*, Degradation mechanism of antibiotics by flower-like

Bi2S3 sensitized anatase/rutile TiO2 coupled with SiO2 photonic crystals, *J. Water Proc. Eng.*, 2024, **58**, 104827, DOI: 10.1016/j.jwpe.2024.104827.

122 N. S. Fuzil, N. H. Othman, N. H. Alias, F. Marpani, M. S. Mat Shayuti, M. Z. Shahruddin, *et al.*, MoS2-TiO2 coated PVDF-based hollow fiber membranes for permeate flux enhancement in membrane distillation, *J. Environ. Chem. Eng.*, 2023, **11**(3), 109866, DOI: 10.1016/j.jece.2023.109866.

123 M. Kazemi, M. Peyravi and M. Jahanshahi, Multilayer UF membrane assisted by photocatalytic NZVI@TiO2 nanoparticle for removal and reduction of hexavalent chromium, *J. Water Proc. Eng.*, 2020, **37**, 101183, DOI: 10.1016/j.jwpe.2020.101183.

124 G. C. Bleier, J. Watt, C. K. Simocko, J. M. Lavin and D. L. Huber, Reversible Magnetic Agglomeration – A Mechanism for Thermodynamic Control over Nanoparticle Size, *Angew. Chem., Int. Ed.*, 2018, **57**, 7678.

125 M. A. Ashraf, W. Peng and Y. Zare, Effects of Size and Aggregation/Agglomeration of Nanoparticles on the Interfacial/Interphase Properties and Tensile Strength of Polymer Nanocomposites, *Nanoscale Res. Lett.*, 2018, **13**, 214, DOI: 10.1186/s11671-018-2624-0.

126 B. Sutariya and S. Karan, A realistic approach for determining the pore size distribution of nanofiltration membranes, *Sep. Purif. Technol.*, 2022, **293**, 121096, DOI: 10.1016/j.seppur.2022.121096.

127 D. Wibowo, F. Mustapa, S. Selviantori, M. Idris, A. Mahmud, M. Maulidiyah, *et al.*, CA/PEG/chitosan membrane incorporated with TiO2 nanoparticles for strengthening and permselectivity membrane for reverse osmosis desalination, *Environ. Nanotechnol. Monit. Manag.*, 2023, **20**, 100848, DOI: 10.1016/j.enmm.2023.100848.

128 T. M. H. Le, R. Wang and S. Sairiam, Self-protecting PVDF-PDA-TiO2 membranes towards highly efficient and prolonged dye wastewater treatment by photocatalytic membranes, *J. Membr. Sci.*, 2023, **683**, 121789, DOI: 10.1016/j.memsci.2023.121789.

129 M. R. Rahman, A. James, K. A. Mohamed Said, M. Namakka, M. U. Khandaker, W. H. Jiunn, *et al.*, A TiO 2 grafted bamboo derivative nanocellulose polyvinylidene fluoride (PVDF) nanocomposite membrane for wastewater treatment by a photocatalytic process, *Mater. Adv.*, 2024, 7617–7636.

130 F. Yan, H. Chen, Y. Lü, Z. Lü, S. Yu, M. Liu, *et al.*, Improving the water permeability and antifouling property of thin-film composite polyamide nanofiltration membrane by modifying the active layer with triethanolamine, *J. Membr. Sci.*, 2016, **513**, 108–116.

131 P. G. Ingole, R. R. Pawar, M. I. Baig, J. D. Jeon and H. K. Lee, Thin film nanocomposite (TFN) hollow fiber membranes incorporated with functionalized acid-activated bentonite (ABn-NH) clay: Towards enhancement of water vapor permeance and selectivity, *J. Mater. Chem. A*, 2017, **5**(39), 20947–20958.

132 M. Shokouhian and S. Solouki, p-Phenylenediamine-grafted multi-walled carbon nanotubes as a hydrophilic modifier in thin-film nanocomposite membrane, *Polym. Bull.*, 2020, **77**(7), 3485–3498, DOI: 10.1007/s00289-019-02899-5.

133 L. L. S. Silva, J. A. Caldara, A. M. Rocco, C. P. Borges and F. V. Fonseca, Evaluation of nano zero-valent iron (nZVI) Activity in solution and immobilized in hydrophilic PVDF membrane for drimaren red X-6BN and bisphenol-a removal in water, *Processes*, 2019, **7**(12), 904, DOI: 10.3390/pr7120904.

134 B. Ozbey-Unal, C. Balcik and B. Van der Bruggen, Development of a novel hydrophilic SiO2/PVDF Janus membrane via different modification methods for robust antiwetting and antifouling membrane distillation, *J. Water Proc. Eng.*, 2023, **54**, 104021, DOI: 10.1016/j.jwpe.2023.104021.

135 Q. Zhao, H. Yang, L. Tong and R. Jin, Pollution Characteristics of Pyrite Surface in Cyanide Tailings by PCA-Assisted ToF-SIMS and Their Correlation with the Contact Angle, *Jom*, 2023, **76**(1), 547–557, DOI: 10.1007/s11837-023-06143-4.

136 M. R. Bilad, E. Guillen-Burrieza, M. O. Mavukkandy, F. A. Al Marzooqi and H. A. Arafat, Shrinkage, defect and membrane distillation performance of composite PVDF membranes, *Desalination*, 2015, **376**, 62–72, DOI: 10.1016/j.desal.2015.08.015.

137 R. Ambedkar, G. Shanker and S. Singh, Investigation of photo-Fenton assisted antibiotic degradation using nZVI/Cu bimetallic heterostructures embedded PVDF film, *Surf. Interfaces*, 2025, **72**, 107122, DOI: 10.1016/j.surfin.2025.107122.

138 J. Mun, H. M. Park, E. Koh and Y. T. Lee, Enhancement of the crystallinity and surface hydrophilicity of a PVDF hollow fiber membrane on simultaneous stretching and coating method, *J. Ind. Eng. Chem.*, 2018, **65**, 112–119, DOI: 10.1016/j.jiec.2018.04.019.

139 A. Siddiqa, H. Razzaq, S. Qaisar, S. Liaqat, M. Arshad and R. Gill, PVDF-Nanodiamonds Composite Membranes: Fabrication, Characterization and Water Treatment Applications, *Der Pharma Chemica*, 2017, **9**(15), 32–40.

140 B. Hao, W. Jarman, H. Peng, K. Li, A. M. Khan, F. Russo, *et al.*, High performance crosslinked polyvinylidene fluoride (PVDF) membranes for solvent permeation, *Membranes*, 2025, **209**, 106174, DOI: 10.1016/j.reactfunctpolym.2025.106174.

141 M. Namakka, MdR. Rahman, M. Sa'don N bt, M. K. B. Bakri and A. Z. Sueraya, Chemisorption and physisorption of polymer nanocomposite membranes, *Polymer Nanocomposite Membranes in Water Treatment and Desalination*, 2025, pp. 423–446, https://www.sciencedirect.com/science/article/abs/pii/B9780443238796000117.

142 A. Z. Sueraya, MdR. Rahman, N. Sa'don M. bt, A. Anak James, M. K. B. Bakri and M. Namakka, Polymer nanocomposite membranes for dye removal, *Polymer Nanocomposite Membranes in Water Treatment and Desalination*, 2025, pp. 187–207, https://

www.sciencedirect.com/science/article/abs/pii/B9780443238796000063.

143 N. Hamzah, C. P. Leo and B. S. Ooi, Superhydrophobic PVDF/TiO2-SiO2 Membrane with Hierarchical Roughness in Membrane Distillation for Water Recovery from Phenolic Rich Solution Containing Surfactant, *Chin. J. Polym. Sci.*, 2019, **37**(6), 609–616.

144 J. Gong, B. Xiang, R. Jin, Z. Li, W. Liu and J. Li, Robust peony-like Cu3(PO4)2/UiO-66-NH2/PVA membranes with exceptional anti-fouling performance for high flux emulsion separation, *Sep. Purif. Technol.*, 2025, **379**, 134915, DOI: 10.1016/j.seppur.2025.134915.

145 K. Xiao, J. Sun, Y. Mo, Z. Fang, P. Liang, X. Huang, *et al.*, Effect of membrane pore morphology on microfiltration organic fouling: PTFE/PVDF blend membranes compared with PVDF membranes, *Desalination*, 2014, **343**, 217–225, DOI: 10.1016/j.desal.2013.09.026.

146 Q. Ma, H. Zhang, X. Deng, Y. Cui, X. Cheng, X. Li, *et al.*, Electrochemical fabrication of NZVI/TiO2 nano-tube arrays photoelectrode and its enhanced visible light photocatalytic performance and mechanism for degradation of 4-chlorphenol, *Sep. Purif. Technol.*, 2017, **182**, 144–150.

147 M. Namakka, MdR. Rahman, N. Sa'don M. bt, M. K. B. Bakri and A. Z. Sueraya, Polymer Nanocomposite Membranes in Water Treatment and Desalination, *Recent Developments, Future Opportunities, and Sustainable Applications*, Woodhead Publishing in Materials, 2025, https://www.sciencedirect.com/science/article/abs/pii/B9780443238796000117.

148 A. Z. Sueraya, M. R. Rahman, K. A. B. M. Said, M. Namakka, D. Kanakaraju, J. Y. Al-Humaidi, *et al.*, Impact of titanium dioxide/graphene in polyvinylidene fluoride nanocomposite membrane to intensify methylene blue dye removal, antifouling performance, and reusability, *J. Appl. Polym. Sci.*, 2024, 1–14.

149 F. G. Ávila, J. Cabrera-Sumba, S. Valdez-Pilataxi, J. Villalta-Chungata, L. Valdiviezo-Gonzales and C. Alegria-Arnedo, Removal of heavy metals in industrial wastewater using adsorption technology: Efficiency and influencing factors, *Clean Eng. Technol.*, 2025, **24**, 100879, DOI: 10.1016/j.clet.2025.100879.

150 A. Kagalkar, S. Dharaskar, N. Chaudhari, V. Vakharia and R. R. Karri, Enhanced metal ion adsorption using ZnO-MXene nanocomposites with machine learning-based performance prediction, *Sci. Rep.*, 2025, **15**(1), 1–26.

151 M. Alimohammady, M. Jahangiri, M. Salavati-Niasari and A. M. Aljeboree, Heavy metal adsorption by graphene oxide modified with 5-amino-3(2-thienyl)pyrazole using central composite design/response surface methodology (CCD/RSM), *RSC Adv.*, 2025, **15**(44), 36837–36860.

152 N. S. Mohamed, M. Abbas and M. Trari, Understanding the rate-limiting step adsorption kinetics onto biomaterials for mechanism adsorption control, *Prog. React. Kinet. Mech.*, 2024, **49**, 1–26.